

AD _____

Award Number: W81XWH-05-1-0278

TITLE: Image Processing and Computer Aided Diagnosis in Computed Tomography of the Breast

PRINCIPAL INVESTIGATOR: Jessie Qing Xia
Joseph Y. Lo, Ph.D.

CONTRACTING ORGANIZATION: Duke University
Durham, NC 27710

REPORT DATE: March 2007

TYPE OF REPORT: Annual Summary

PREPARED FOR: U.S. Army Medical Research and Materiel Command
Fort Detrick, Maryland 21702-5012

DISTRIBUTION STATEMENT: Approved for Public Release;
Distribution Unlimited

The views, opinions and/or findings contained in this report are those of the author(s) and should not be construed as an official Department of the Army position, policy or decision unless so designated by other documentation.

| REPORT DOCUMENTATION PAGE | | | | Form Approved OMB No. 0704-0188 | |
|--|-------------|----------------------------------|----------------------------|--|---|
| Public reporting burden for this collection of information is estimated to average 1 hour per response, including the time for reviewing instructions, searching existing data sources, gathering and maintaining the data needed, and completing and reviewing this collection of information. Send comments regarding this burden estimate or any other aspect of this collection of information, including suggestions for reducing this burden to Department of Defense, Washington Headquarters Services, Directorate for Information Operations and Reports (0704-0188), 1215 Jefferson Davis Highway, Suite 1204, Arlington, VA 22202-4302. Respondents should be aware that notwithstanding any other provision of law, no person shall be subject to any penalty for failing to comply with a collection of information if it does not display a currently valid OMB control number. PLEASE DO NOT RETURN YOUR FORM TO THE ABOVE ADDRESS. | | | | | |
| 1. REPORT DATE 01-03-2007 | | 2. REPORT TYPE Annual Summary | | 3. DATES COVERED 1 Mar 2006 – 28 Feb 2007 | |
| 4. TITLE AND SUBTITLE Image Processing and Computer Aided Diagnosis in Computed Tomography of the Breast | | | | 5a. CONTRACT NUMBER | |
| | | | | 5b. GRANT NUMBER W81XWH-05-1-0278 | |
| | | | | 5c. PROGRAM ELEMENT NUMBER | |
| 6. AUTHOR(S) Jessie Qing Xia Joseph Y. Lo, Ph.D. Email: qing.xia@duke.edu | | | | 5d. PROJECT NUMBER | |
| | | | | 5e. TASK NUMBER | |
| | | | | 5f. WORK UNIT NUMBER | |
| 7. PERFORMING ORGANIZATION NAME(S) AND ADDRESS(ES) Duke University Durham, NC 27710 | | | | 8. PERFORMING ORGANIZATION REPORT NUMBER | |
| 9. SPONSORING / MONITORING AGENCY NAME(S) AND ADDRESS(ES) U.S. Army Medical Research and Materiel Command Fort Detrick, Maryland 21702-5012 | | | | 10. SPONSOR/MONITOR'S ACRONYM(S) | |
| | | | | 11. SPONSOR/MONITOR'S REPORT NUMBER(S) | |
| 12. DISTRIBUTION / AVAILABILITY STATEMENT Approved for Public Release; Distribution Unlimited | | | | | |
| 13. SUPPLEMENTARY NOTES Original contains colored plates: ALL DTIC reproductions will be in black and white. | | | | | |
| 14. ABSTRACT Dedicated breast CT imaging is a promising technique for breast cancer imaging. Since it can totally remove the overlapping of tissues, it will be even more beneficial for women with dense breasts. Still, there is a lot to be done for advancing the breast CT technology. One direction of development is to improve the image quality via some post-acquisition processing techniques, which is the goal of this project. Specifically, two subtasks are considered: 1) to remove scattered radiation, and 2) to remove noise. So far, the Gaussian noise model has been proposed and the corresponding Bayesian version is constructed for scatter compensation. A PDEtomo denoising technique has been proposed and implemented which takes into account the relationship between the variance of line integrals through different region of breast and the number of photons hitting the detector. Results show that they are effective for the specific tasks. In addition, some other techniques are being explored or under further evaluation. The project has progressed to the stage where a computer aided diagnosis tool is under development for the assessment of mass detectability based on the original breast CT volumes and those with image processing. | | | | | |
| 15. SUBJECT TERMS breast imaging, breast CT, scatter compensation, denoising, CAD, Cone-beam CT | | | | | |
| 16. SECURITY CLASSIFICATION OF: | | | 17. LIMITATION OF ABSTRACT | 18. NUMBER OF PAGES | 19a. NAME OF RESPONSIBLE PERSON |
| a. REPORT | b. ABSTRACT | c. THIS PAGE | | | USAMRMC |
| U | U | U | UU | 53 | 19b. TELEPHONE NUMBER (include area code) |

Table of Contents

Introduction..... 1

Body..... 1

Key Research Accomplishments..... 5

Reportable Outcomes..... 5

Conclusions..... 6

References..... 6

Appendices..... 8

Introduction

Breast cancer is the second most common cancer type affecting American women. The disease is also the second leading cause of cancer-related death for American women, which was predicted to kill 40,460 women in 2007.¹ Presently there is no effective way of preventing the disease. However, the detection of the cancer at its early stage has been found to significantly improve the survival rates²⁻⁵. Moreover, there are more treatment options for a patient with earlier stage cancer than whose with a late stage of cancer⁶⁻⁸.

Film-screen X-ray mammography is still the only FDA approved screening tool aiming at early detection of the breast cancer. While it has been proven to be effective, it is not omnipotent in its detection sensitivity of breast lesions due to several limitations such as two-dimensional (2D) projection data acquisition and restricted range of linear optical response of the detector. For women with dense breasts, the sensitivity is lower since in their mammograms the dense appearance of the breast tissue is more likely to obscure any abnormalities and makes the detection of breast cancer even more challenging⁹.

With the development of flat-panel detectors in recent years, the dedicated cone-beam CT technology became feasible. By tomographic reconstruction, the issue of tissue overlapping is solved. The technology is potentially advantageous for women with dense breasts. A research group in University of California Davis is currently conducting clinical trials.¹⁰ The reconstructed volumes of human subjects provide exciting new 3D information about breasts that is never seen before. Yet, at its early stage of development, breast CT technology need to be advanced.

What this project is addressing is the post-acquisition image processing techniques to improve the reconstructed breast CT image quality. Firstly, the raw projection images of breast CT are acquired without using an anti-scatter grid. The residual scattered radiation in the projections has to be reduced via some post-acquisition techniques. Secondly, the breast CT data are obtained with the same dose as the standard two-view mammography. When this level of dose is equally split into around 500 projections, each projection contains considerable noise. So does the reconstructed volume. Therefore, it is desirable to have some image processing tools for noise removal.

The proposed project is a collaborative effort between our group at Duke and Dr. Boone's group in University of California Davis. Based on the raw data provided by them, we will develop the techniques for image improvement via the scatter compensation and/or denoising.

Report Body

Task 1: Develop and test a unique two-dimensional Bayesian image processing technique on the projection data of cone-beam breast Computed Tomography (breast CT) obtained without a grid.

This task has been completed and the results are incorporated into the papers listed under the category of reportable outcomes. This task is split into two subtasks. The first subtask

is to develop an algorithm for scattered radiation removal. The second subtask is to reduce the quantum noise from breast CT data.

Firstly, an algorithm is designed and implemented for scatter reduction. To account for the energy-integrating characteristic of the flat-panel digital detector, Gaussian distributions are used to approximate the signals recorded at individual pixels of the detector. For the task of removing scattered radiation, the Gaussian noise model is proposed. The Maximum Likelihood Estimator (MLE) is obtained via an Expectation Maximization algorithm in an iterative manner. As the image is processed through many iteration steps, the high frequency noise in the image will be also amplified. In order to suppress this side effect, the Maximum A Posteriori (MAP) estimator is obtained by combining the Gaussian noise model with a Gibbs prior via Bayes rule. It is calculated by the procedure proposed by Hebert and Leahy¹¹.

Figure1 shows the comparison between the original image and MAP estimate of the scatter-free image. Table 1 is the residual scatter fraction (RSF) and contrast to noise ratio (CNR) measurements on these three images. It is shown that with our algorithm, the scattered radiation on the images acquired without a grid can be reduced down to the level achieved by using a grid. Meanwhile, the CNR of the processed image is twice that of the image acquired with a grid.

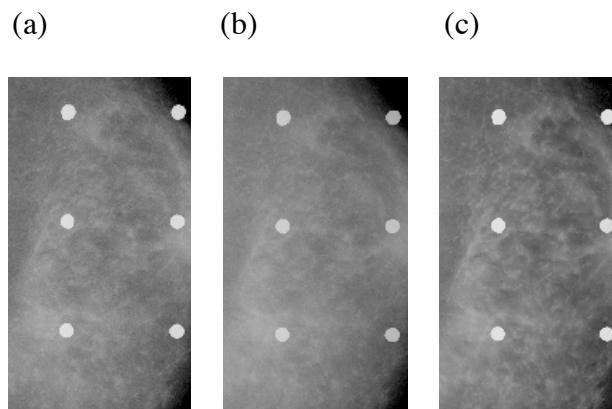


Figure 1: Radiographs of an anthropomorphic breast phantom acquired on Siemens prototype FFDM system (a) with and (b) without an anti-scatter grid; (c) the MAP algorithm processed image based on (b). The white disks are the beam stop (made of lead) array for scatter radiation measurement.

Table 1: Corresponding residual scatter fraction (RSF) and contrast to noise ratio (CNR) results for the three images shown in Figure 1.

| | With grid | Without grid | Without grid; scatter reduction |
|------------|-----------|--------------|---------------------------------|
| RSF | 11% | 45% | 10% |
| CNR | 7.04 | 6.99 | 15.29 |

Secondly, a partial-diffusion-equation based denoising technique was developed for noise removal in breast CT. It is observed that the line integral images (converted from the raw images by logarithmic operation) have the following property: line integrals through the center of the breast have much higher variance than those through the edge of the breast.

We derived a theoretical formula between the line integral variance and the number of photons hitting the detector for a specific pixel region: $\text{var}(l_{ij}) \cong \frac{1}{\lambda_{ij}}$. The details of the derivation can be found in the paper corresponding to reportable outcome #1. Based on this formalism we propose a PDE_{tomo} (abbreviation for: PDE for tomography/tomosynthesis) algorithm for breast CT data.

Task 2: Reconstruct the three-dimensional breast image based on the processed projection data from Task 1.

This task has already been completed and some results are shown in the reportable outcome #1. A Feldkamp-type filtered back projection (FBP) algorithm¹² was custom-written and used for the cone-beam reconstruction of the breast CT data.

For the results shown in Figure 2, the PDE_{tomo} technique was applied to the line integral images converted from raw projections. The processed projection images were then fed into the FBP core for reconstruction. The reconstructed breast CT volume provides unique anatomic information of the breast that is not available before. In addition, the PDE_{tomo} technique is very effective in removing the noise while maintaining the details.

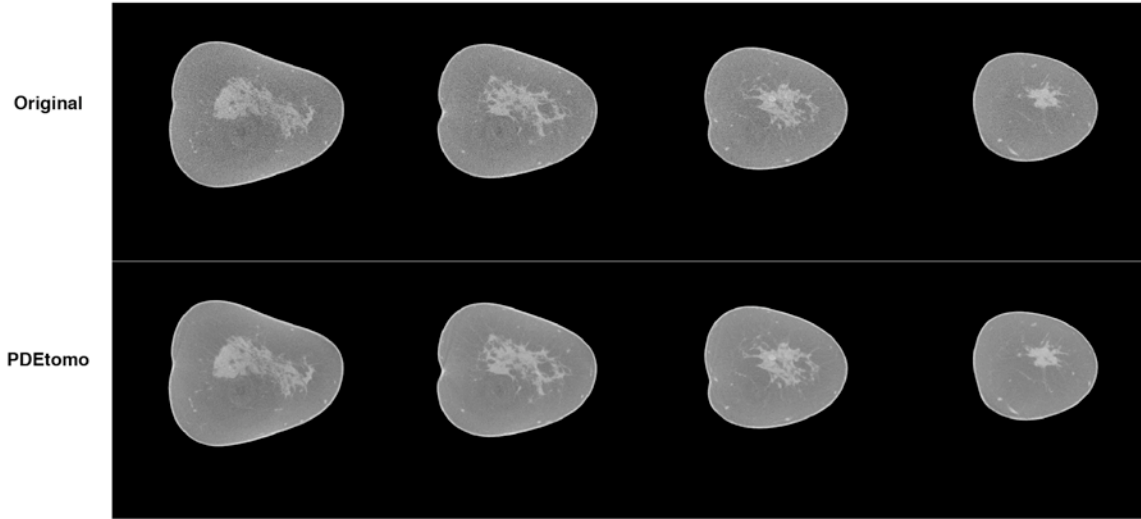


Figure 2: Reconstructed coronal sections of a breast of a human subject. The section thickness is 0.5mm. The top row is derived with the original dataset. The bottom row is derived with the PDE_{tomo} processed dataset. It is manifest that PDE_{tomo} processed volume has remarkable less noise than the original volume.

Task 3: Apply the algorithm in Task 1 to the two-dimensional slices of the reconstructed three-dimensional breast image from the unprocessed projection data.

This task has been completed. A two-dimensional PDE denoising technique (denoted by PDE_{2D}) was developed and coded.

The PDE_{2D} algorithm was applied after reconstruction on each of the reconstructed slices to remove the noise. By contrast, the PDE_{tomo} technique presented in Task 1 is intrinsically a three-dimensional technique, which is applied to the projection images before tomographic reconstruction. The results of these two techniques are compared with each other. One such example is shown in Figure 3. Figure 3(a) is the same slice as shown in #2 in the bottom row of Figure 2. That is, the volume was processed by the PDE_{tomo} algorithm. Figure 3(b) is the one processed by PDE_{2D} algorithm. The parameters of the techniques are adjusted such that they have about the same level of noise within the fatty tissue region. However, Figure 3(a) has much better anatomical depiction than Figure 3(b). The likely explanations for this are as follows. Because the existence of the noise (both quantum noise and electronic noise) in the projection images, some anatomical details are lost during tomographic reconstruction. By removing the noise first, as the PDE_{tomo} technique does, some anatomical details can be recovered. By contrast, since PDE_{2D} technique is used after FBP reconstruction, it cannot restore the lost anatomical detail information. Thus, we concluded that the denoising strategy in this specific task is inferior to the one in Task 1.

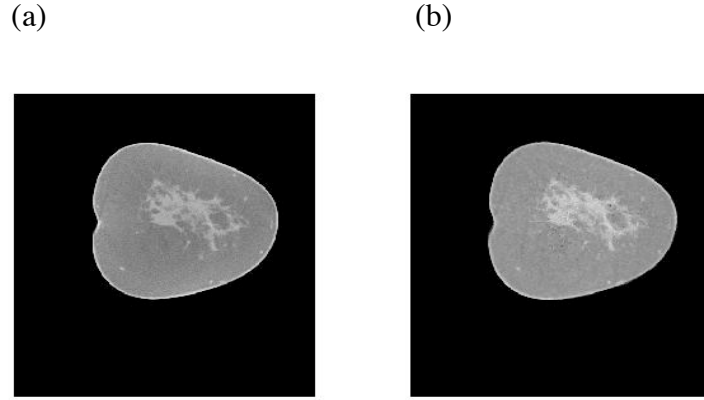


Figure 3: Processed and reconstructed coronal sections of the same breast as in Figure 2, using the denoising strategies in (a) Task1 and (b) Task3, respectively. The two slices have approximately the same level of noise removal. The one on the left shows more anatomical details than the one on the right.

Task 4: Develop and test three-dimensional Bayesian image-processing technique on the reconstructed image based on the unprocessed projection data acquired without a grid.

This task has almost been completed. A three-dimensional PDE technique (PDE_{3D}) has been developed and is currently under further evaluation. The PDE_{3D} technique differs from PDE_{2D} in that it has a three-dimensional neighborhood system.

In addition, we are exploring a PDE_{3D} counterpart to be applied before tomographic reconstruction.

This task should be completed within half a month.

Task 5: Develop a Computer Aided Diagnosis tool for detecting breast mass lesions based on the projection data.

This task is a work in progress. Some preliminary work has been done.

The 20 human volunteer datasets were requested from the collaborating group in University of California Davis. The breast volumes were reconstructed for each case. Then the afore-mentioned PDE_{tomo} technique was applied to the breast CT datasets as described in Task2.

A computer-based virtual x-ray CT imager is developed. It uses the same parameters as the physical breast CT system. A routine for simulation of masses with random shape is also written. Putting the simulated mass into the virtual imager, the projection images can be obtained. The simulated projection images with known mass are then obtained by summing up the projection images from the virtual imager and the clinical projection images.

The CAD tool based on signal known exactly (SKE) scenario is under development.

Task 6: Test and compare the performances of the CAD developed in Task 5 applied to processed projection data from Task 1 with the CAD performance on the projection data without Bayesian processing.

Once the CAD in task 5 is completely developed, this task will be carried out to compare the CAD performances on original and processed datasets.

Key Research Accomplishments

- Proposed and developed the Gaussian noise model;
- Proposed and developed a PDE_{tomo} algorithm for volume denoising in breast CT;
- Clinical breast CT data have been reconstructed;
- Application of the PDE_{tomo} algorithm on simulation data and clinical data has shown improvement of image quality using CNR and resolution as figures of merit.
- Developed PDE_{2D} and PDE_{3D} techniques;
- A virtual breast CT imager was developed.
- A routine for 3D mass simulation with random shape was written.

Reportable Outcomes

Two publications were resulted from this project in the second fiscal year, including a peer-reviewed paper and a conference proceeding. They are attached to the end of the report as appendices. Both the name of PI (Jessie Q. Xia) and the name of the advisor (Joseph Y. Lo) are bolded.

1. **Jessie Q. Xia, Joseph Y. Lo,** Kai Yang, Carey E. Floyd Jr., John M. Boone, Dedicated Breast CT: Volume Image Denoising via a Partial Diffusion Equation Based Technique. *Medical Physics* (submitted).
2. **Jessie Q. Xia,** Georgia D. Tourassi, **Joseph Y. Lo,** Carey E. Floyd Jr., On the Development of a Gaussian Noise Model for Scatter Compensation. *Proceedings of SPIE Medical Imaging 2007* (in press).

Conclusions

Dedicated breast CT imaging is a promising technique for breast cancer imaging. Since it can totally remove the overlapping of tissues, it will be even more beneficial for women with dense breasts.

Still, there is a lot to be done for advancing the breast CT technology. One direction of development is to improve the image quality via some post-acquisition processing techniques, which is the goal of this project. Specifically, two subtasks are considered: 1) to remove scattered radiation, and 2) to remove noise. So far, some techniques have been designed and developed, and results show that they are effective for the specific tasks.

The project has progressed to the stage where a computer aided diagnosis tool is under development for the assessment of mass detectability based on the original breast CT volumes and those with image processing.

References

1. ACS, "American Cancer Society: Cancer Facts and Figures 2005," Atlanta, Ga: American Cancer Society (2005).
2. I. Reiser, R. M. Nishikawa, M. L. Giger, T. Wu, E. Rafferty, R. H. Moore and D. B. Kopans, "Computerized detection of mass lesions in digital breast tomosynthesis images using two- and three dimensional radial gradient index segmentation," *Technology in Cancer Research & Treatment* **3**, 437-441 (2004).
3. C. E. Floyd, Jr, J. Y. Lo and G. D. Tourassi, "Cased-based reasoning computer algorithm that uses mammographic findings for breast biopsy decisions," *AJR. American Journal of Roentgenology* **175**, 1347-1352 (2000).
4. H. P. Chan, J. Wei, B. Sahiner, E. A. Rafferty, T. Wu, M. A. Roubidoux, R. H. Moore, D. B. Kopans, L. M. Hadjiiski and M. A. Helvie, "Computer-aided diagnosis system for breast masses on digital tomosynthesis mammograms: Preliminary experience," *Radiology* **238**, 1075-1080 (2006).
5. V. L. Ernster, J. Barclay, K. Kerlikowske, H. Wilkie and R. Ballard-Barbash, "Mortality among women with ductal carcinoma in situ of the breast in the population-based surveillance, epidemiology and end results program," *Archives of Internal Medicine* **160**, 953-958 (2000).
6. G. Dave, H. Cosmatos, T. Do, K. Lodin and D. Varshney, "Metaplastic carcinoma of the breast: A retrospective review," *INTERNATIONAL JOURNAL OF RADIATION ONCOLOGY BIOLOGY PHYSICS* **64**, 771-775 (2006).
7. R. W. Sahoo S, Jaskowiak N, Tong LP, Heimann R, "Defining negative margins in DCIS patients treated with breast conservation therapy: The University of

- Chicago experience," BREAST JOURNAL 11 (4): 242-247 JUL-AUG 2005 (2005).
8. S. Joslyn, "Ductal carcinoma in situ: Trends in geographic, temporal, and demographic patterns of care and survival," BREAST JOURNAL 12 (1): 20-27 JAN-FEB (2006).
 9. V. P. Jackson, R. E. Hendrick, S. A. Feig and D. B. Kopans, "Imaging of the Radiographically Dense Breast," Radiology **188**, 297-301 (1993).
 10. J. Boone, "Performance assessment of a pendant-geometry CT scanner for breast cancer detection," Proc. SPIE (2005).
 11. R. Hebert, T. Leahy, "A generalized EM algorithm for 3-D Bayesian reconstruction from Poisson data using Gibbs priors," Medical Imaging, IEEE Transactions on **8**, 194-202 (1989).
 12. L.A. Feldcamp, L.C. Davis JW Kress, "Practical cone-beam algorithm," Journal of the Optical Society of America a-Optics Image Science and Vision **1**, 612-619 (1984).

Appendices

The Medical Physics and SPIE manuscripts are attached, see "Reportable Outcomes" above for the list.

Appendix

Jessie Q. Xia, Joseph Y. Lo, Kai Yang, Carey E. Floyd Jr., John M. Boone, Dedicated Breast CT: Volume Image Denoising via a Partial Diffusion Equation Based Technique. *Medical Physics (submitted)*.....9

Jessie Q. Xia, Georgia D. Tourassi, Joseph Y. Lo, Carey E. Floyd Jr., On the Development of a Gaussian Noise Model for Scatter Compensation. *Proceedings of SPIE Medical Imaging 2007 (in press)*.....41

Dedicated Breast Computed Tomography: Volume Image Denoising via A Partial-Diffusion Equation Based Technique

5 Jessie Q. Xia^{1,2}, Joseph Y. Lo^{1,2,3}, Kai Yang⁴, Carey E. Floyd, Jr.^{1,2,3} and John M.
Boone^{4,5}

¹ Department of Biomedical Engineering, Duke University, Durham, NC 27708

² Duke Advanced Imaging Laboratories, Department of Radiology, Duke University Medical Center, Durham, NC 27705

10 ³ Medical Physics Graduate Program, Duke University Medical Center, Durham, NC 27708

⁴ Department of Biomedical Engineering, University of California Davis, Davis, CA 95616

15 ⁵ Department of Radiology, University of California Davis Medical Center, Sacramento, CA 95817

Abstract:

Dedicated breast CT imaging possesses the potential for improved lesion detection over conventional mammograms, especially for women with dense breasts. The breast CT
20 images are acquired with a glandular dose comparable to that of standard two-view mammography for a single breast. Due to dose constraints, the reconstructed volume has a non-negligible quantum noise when thin section CT slices are visualized. It is thus desirable to reduce noise in the reconstructed breast volume without loss of spatial resolution. In this study, a partial-diffusion equation (PDE) based denoising technique
25 specifically for breast CT was developed and applied on the projection data prior to reconstruction. Simulation results show that the PDE technique outperforms Wiener denoising. At the photon fluence level of 2.5×10^4 for each projection, the noise of PDE denoised image was 39.3% of Wiener denoised images, while the resolution was higher. The PDE technique increases its performance advantage relative to Wiener techniques

30 when the photon fluence is reduced. For subjective evaluation, the PDE technique was applied to two human subject breast datasets acquired on a prototype breast CT system. The denoised images had appealing visual characteristics with much lower noise levels and improved tissue textures while maintaining sharpness of the original reconstructed volume.

35

Keywords: breast imaging, breast CT, PDE, volume noise removal

Running Title: PDE based volume image denoising in breast CT

Introduction

40 The most common cancer type that affects women globally other than skin cancer is breast cancer ¹. Moreover breast cancer is a leading cause of cancer-related women mortality, secondary only to lung cancer. It is estimated that the disease will kill about 40,460 US women in 2007 ¹. Although mammography is the standard clinical screening technique ^{2,3} for breast imaging, superimposition of normal anatomical structures may
45 potentially obscure a breast lesion. The situation gets even worse for women with dense breasts ⁴, which have more anatomical noise in the projection image. Researchers are developing alternative x-ray breast imaging techniques that may overcome the limitations of mammography, including three-dimensional imaging techniques such as breast tomosynthesis ^{5,6} and dedicated breast CT ⁷⁻¹².

50 Not long after the CT technique was invented in 1972, a group of researchers studied breast CT imaging ¹³. They applied the whole-torso-scanning mode and found that a high patient dose was needed to achieve adequate image quality. With the advent of high-resolution flat-panel detectors at the end of the 1990s, the concept of breast CT once again came into researchers' horizon. In particular, a 2001 paper ⁷ showed that dedicated
55 breast CT could achieve quality breast images with dose levels comparable with two-view mammography for the same breast.

Preliminary human subject data acquired on our first prototype breast CT system ¹⁴ provide exciting new information of the breast that was not available in the past. However, because the relatively low total dose must be split among a large number of
60 projection views (around 500), reconstructed breast CT thin sections contain considerable quantum noise. Thus it is desirable to reduce noise levels to improve the conspicuity of

breast lesions. At the same time, it is desirable to retain spatial resolution. Alternatively, by applying denoising techniques, the gain of improving CT image quality can be exchanged for dose reduction while maintaining the image quality.

65 For low dose CT, some general-purpose sinogram smoothing techniques based on either penalized likelihood ¹⁵ or penalized weighted least squares ¹⁶ were developed. These techniques can be potentially applied on dedicated breast CT datasets. Zhong et al ¹⁷ developed a wavelet-based technique and applied it on phantom breast CT data. Their results showed that with denoising, dose could be potentially reduced by up to 60%.

70 The Partial Diffusion Equation (PDE) based technique ^{18, 19} is another state-of-the-art denoising method which is effective not only in removing noise but also in preserving detail. Although computationally intensive, this iterative method can provide more freedom in choosing the desired denoising effect. In this study, we describe a PDE based denoising technique specifically for breast CT and evaluate it both on simulated and
75 empirically collected human subject datasets.

The image quality of PDE denoised images was compared against that of standard Weiner filtering techniques. Quantitative comparisons were made using simulated data at various exposure levels, while qualitative comparisons were made using dedicated breast CT scan data from two human subjects.

Materials and Methods

85 **Dedicated Breast CT System and Human Subject Datasets**

As is illustrated in Figure 1, dedicated breast CT systems are typically designed as follows: a patient lies supine on a lead-shielded table with one breast hanging through a hole on the table in the pendant geometry. The x-ray tube and the flat panel detector rotate in the horizontal plane underneath the table. This setup is different from a
90 conventional CT system, where the x-ray tube and detector rotate around the torso of a patient (axial scanning). Since only the breast to be imaged is exposed to the x-ray beam, the dose to the patient can be greatly reduced. A pilot study ⁷ showed that this type of dedicated breast CT system is able to achieve a satisfactory image quality with dose levels comparable to standard two-view mammography for the same breast.

95 Using the above system design, a custom-designed breast CT system was fabricated at the University of California Davis Medical Center, and is currently accruing patient images. The x-ray tube has a Comet beryllium-windowed, water-cooled tungsten anode and a nominal focal spot with the size of 0.4 mm x 0.4 mm. A Pantak high frequency x-ray generator drives the tube with the voltage ranging from 10 kV to 110 kV. The CsI-
100 based flat panel detector (Varian, PaxScan 4030CB) has a field of view of 40 cm x 30 cm. Using 30 frames per second and 2 x 2 pixel binning mode, the detector generates the images each with matrix size of 1024 x 768 and pixel dimension of 0.388 mm x 0.388 mm. A Kollmorgen servo motor was employed to drive the rotation of the tube-detector gantry as well as encode the angular information. The source-to-isocenter distance is 46.9
105 cm and the source-to-detector distance is 88.4 cm.

For the two human subject datasets presented in this paper, the projection images were acquired under 80 kVp using a circular orbit. The mAs values were chosen for each subject such that the mean glandular dose using breast CT was equal to two-view mammography. Each subject is scanned within 17 seconds to get a total of 500 projection
 110 images that span slightly over 360 degrees. After dead pixel and flat field corrections, each dataset is ready for tomographic reconstruction.

Simulated Breast CT Datasets

In this study, some simulated breast CT datasets were also generated to aid the analysis. The computer-generated breast is a hemisphere with radius of 7cm. It has homogeneous
 115 breast tissue with a uniform linear attenuation coefficient of 0.28 cm^{-1} and is surrounded by 1mm thick skin ²⁰ with linear attenuation coefficient of 0.5 cm^{-1} . A spherical lesion with 10% contrast relative to the breast tissue was embedded at the center of the breast. This simulated breast was scanned virtually by a monochromatic x-ray cone beam with infinitely small focal spot and ideal flat-panel detector with 100% detective quantum
 120 efficiency. The geometric parameters are the same as the physical breast CT scanner described in the previous subsection.

For each 2D projection image, an analytical line integral image was first obtained based on the aforementioned virtual dedicated breast CT scanning. A noisy raw image was generated according to the measurement model ²¹. The model takes into account both
 125 photon quantum noise and electronic read-out noise. It has the following form:

$$Y_i = G_i \bar{E} \cdot \text{Poisson}(I_0 e^{-l_i}) + \text{Gaussian}(0, \sigma^2), \quad (1)$$

where G_i is the gain factor of the imaging system, \bar{E} is the mean energy level of the polychromatic x-ray beam, and the Gaussian term is for the electronic noise. In our

simulation we chose $G_i=0.0035$ /keV, $\bar{E}=40$ keV, and $\sigma^2=10$. The values of G_i and σ^2 were referred to those used in ²¹.

Tomographic Reconstruction

Before reconstruction, the raw projection images undergo a preprocessing step. The simplest preprocessing step is to convert the raw projection image into the line integral via the logarithm operation. On each raw projection image, a region of interest (ROI) is identified which is outside the breast silhouette, and the pixel value without attenuation I_0 is approximated by the mean pixel value with the ROI. Then the line integral image is obtained by: $l_{ij} = \log(I_0 / I_{ij})$, where I_{ij} is the pixel value at (i, j) position.

Since the datasets have high angular sampling rate, the computationally efficient filtered backprojection (FBP) ²² algorithm was chosen for reconstruction. The Feldkamp type FBP for cone-beam geometry was custom written and a Shepp-Logan filter was used.

PDE Denoising Technique

The PDE denoising strategy was inspired by the heat equation, which characterizes the spatial temperature distribution as a function of time. When the time period is very long, the temperatures tend to be uniform in space, i.e., the temperature image is smoothed. Therefore, if an image needs to be denoised, it can be treated as a temperature image and fed into the heat equation for its smoothed versions as time goes by. The simplest case will be the heat propagation in a homogenous media, or equivalently, smoothing equally all over the space. The heat equation in this case will be:

$$\frac{\partial I}{\partial t} = k \nabla^2 I = \nabla \cdot (k \nabla I), \quad (2)$$

where k is a scalar diffusivity constant of the homogeneous media, ∇I is the gradient of the image I and $\nabla^2 I = \nabla \cdot (\nabla I)$ is the Laplace operation on I over the spatial variables ²³.

This simplest case will smooth out both the noise and the detail such as the edges in the image. However, a nonlinear PDE can reduce noise while preserving spatial resolution in the image:

$$155 \quad \frac{\partial I}{\partial t} = \nabla \cdot (p(|\nabla I|) \nabla I), \quad (3)$$

where $p(\cdot)$ is called the diffusivity function, a function of the gradient norm $|\nabla I|$. Equation (2) is a special case of Equation (3) where $p(\cdot)$ is chosen to be a constant value k . The $p(\cdot)$ named diffusivity is a function to regulate the local smoothness. The choice of $p(\cdot)$ is critical to PDE-based denoising of images. In this work, we chose a diffusivity function

160 proposed by Perona and Malik ¹⁸:

$$p(d) = e^{-\frac{d^2}{\delta^2}} \quad (4)$$

where δ is a user-specified parameter. When the image gradient norm is very large at a location region, the diffusivity will be very small, and thus the local image values will be preserved within a small time period whereas another more uniform region will be smoothed out at the same time. The parameter δ acts like a cut-off value; image regions with gradient norm below δ will have more noise removed while regions with a higher gradient norm will stay sharp.

The diffusion equation can be discretized by the finite difference approach using the first-order neighborhood system. Each pixel has four neighbors: the north, south, west and east neighbor pixels. Assuming $\Delta x = \Delta y = 1$ in the two-dimensional case, the discretized version of Equation (3) is

$$170 \quad \frac{I_{ij}^{t+1} - I_{ij}^t}{\Delta t} = [p_N \cdot \nabla_N I + p_S \cdot \nabla_S I + p_W \cdot \nabla_W I + p_E \cdot \nabla_E I]_{ij}^t \quad (5)$$

where Δt is discretized time step, $[p_N, p_S, p_W, p_E]$ are the values of the diffusivity function at the neighboring pixels of location I_{ij} , and $\nabla_* I$ is a notation for the difference between

175 the pixel value of one neighbor and I_{ij} itself. In this work, $\Delta t = 0.1$ was used.

The simulated breast CT data revealed a pattern of noise on its line integral images. That is, toward the chest wall of the breast the noise is larger. When the photon fluence is reduced, the phenomenon becomes even more obvious. A line profile is shown in Figure 2 to help illustrate this point. It can be explained theoretically. Again, a simplifying

180 assumption of monochromatic beam is used. If

$$I_{ij} \sim \text{Poisson}(\lambda_{ij})$$

$l_{ij} = \log \frac{I_0}{I_{ij}} = \log I_0 - \log I_{ij}$, then the variance of the line integral l_{ij} can be approximated

by the delta method²⁴ using the second-order Taylor expansion:

$$\text{var}(l_{ij}) = \text{var}(\log I_{ij}) \cong \text{var}(I_{ij}) * [f'(\log I_{ij})]^2 \cong \frac{1}{\lambda_{ij}}. \quad (6)$$

This formalism can be integrated into the PDE denoising technique by adapting the
185 parameter δ in the diffusivity function spatially as:

$$\delta_{ij} \propto \sqrt{\text{var}(l_{ij})}. \quad (7)$$

The resultant PDE denoising technique is denoted PDE for Tomography/Tomosynthesis (PDEtomo).

The PDE denoising method can be applied to the CT data at different points in the
190 reconstruction process. When a Filtered backprojection (FBP) algorithm is used for reconstruction, there are four potential locations where the denoising techniques can applied, which are illustrated in Figure 3. In this study, the denoising techniques were

applied at step 2. That is, the line integral images are processed and these denoised data were used in the FBP algorithm.

195 The datasets were also processed by Wiener adaptive filtering technique commercially implemented by MATLAB (Mathworks Inc, Natick, Massachusetts), for comparison.

Image Evaluation

Contrast of the lesion, noise level, contrast-to-noise ratio (CNR) and resolution²⁵ are metrics for the quantitative evaluation of the denoising technique. These metrics were
200 calculated based on the reconstructed slices of the simulated breast. The contrast of the lesion is defined as the relative difference between the average pixel values within the lesion and those outside the lesion. The noise level is characterized by the percent noise, that is, the standard deviation of the pixel values within a uniform ROI relative to the mean value. This is also called the coefficient of variation (COV). The CNR measure is
205 the ratio of contrast of the lesion to the percentage noise, which is equivalent to the signal to noise ratio (SNR).

In order to measure spatial resolution, a high intensity sphere was simulated within the breast, projected, and target reconstructed (with an in-plane pixel dimension of 0.2mm) around the high-intensity sphere. Then the edges of the circular disc within a
210 reconstructed slice are averaged radially. For each specific denoising technique, a Gaussian function is fitted to the edge, and the full width at half maximum (FWHM) of that function was measured as the parameter to evaluate the spatial resolution.

Results

Simulation Results

215 In Figure 4, the three columns correspond to the reconstructed slices of the simulated breast CT data without denoising, with Wiener denoising and with the PDEtomo denoising, respectively. The four rows show the results using varying photon fluences using $I_0=2.5e3$, $5e3$, $7.5e3$ and $2.5e4$ correspondingly from the top to the bottom. The noise level is appreciably lower for each successive row. The reconstructed slice
220 thickness was 0.5 mm and within-plane pixel dimension was 0.8 mm. These slices contain a lesion at the center, which is only barely visible for the highest fluence level (bottom panel). With Wiener processing, the lesion is visible for the highest two fluence levels. With PDEtomo processing, the lesion is visible for the highest three fluence levels. To demonstrate the effect of denoising on the uniformity of the noise level across the
225 image, another reconstructed coronal view slice containing only homogeneous breast tissue is shown in Figure 5(a). For the horizontal center line, the standard deviation of a local 7x7 ROI centered at each pixel on that horizontal line is plotted in Figure 5(b) to (d) for photon fluence of $2.5e3$, $5e3$ and $2.5e4$.

In all three cases, the original image, as shown on the left of Figure 5(a), presents a non-
230 uniform level of noise such that the interior section has higher standard deviation values, that is, higher noise levels than the periphery. Wiener processing reduces the overall noise level, but the non-uniform trend remains in Figure 5(b) and 6(c) corresponding to lower photon fluences. The PDEtomo processed images reduce the noise and also the non-uniformity of the plot. For the highest fluence images in Figure 5(d), the effects of
235 Wiener and PDEtomo denoising are very similar.

The CNR results based on the images depicted in Figure 4 are given in Figure 6. At the highest fluence of 2.5×10^4 , CNRs of the Wiener and PDEtomo processed images are 3.59 and 4.08 times that of the original one, respectively. The paired two-tailed student t test of CNRs of the Wiener and PDEtomo results gives the p-value of 0.0036, indicating that the CNRs of PDEtomo were statistically higher than those of Wiener. Similar trends were observed at the lower fluence levels.

The resolution results are given in Figure 7. The first image in the top panel shows the full view reconstructed slice with a high-intensity sphere embedded into the center of the breast tissue. The ROI for targeted reconstruction is marked on the slice. The original reconstructed slice as well as the wiener denoised one are to the right of the first row of Figure 7(a).

In the second row, the PDEtomo denoised result is shown in the middle. To its left, a Gaussian kernel is directly applied to the original target-reconstructed slice and its resultant blurred slice obtains the same noise level as the PDEtomo result. To its right, a corresponding Gaussian blurred one obtains the same resolution level. As a comparison, the PDEtomo achieves a low noise level and the high resolution simultaneously. In Figure 7(b), the noise and resolution values are obtained and plotted for both the PDEtomo and Wiener techniques. As shown in the noise-resolution plot, PDEtomo processing outperforms Wiener processing because it has lower noise and higher resolution. The noise levels of the Wiener and PDEtomo techniques are 12.0% and 4.7%, respectively. The noise level of Wiener is 2.54 times that of the PDEtomo. At the same time, the resolution measure was 0.2209 mm for PDEtomo and 0.2867 mm for Wiener. The resolution of PDEtomo is better than that of Wiener.

260 **Human Subject Results**

Figure 8 and 9 show the coronal reconstructed slices from two human subject breast CT data. By visual comparison, PDEtomo technique (bottom row) reduces the noise considerably while maintaining the resolution of the original reconstruction (top row).

265

Discussion

Dedicated breast CT imaging is an exciting new candidate that possesses the potential of improving breast cancer diagnosis over conventional mammography. Some preliminary studies^{14, 26, 27} show that satisfactory images can be acquired using the same dose as standard two-view mammography. When this dose is divided among the potentially hundreds of individual projection images comprising each scan, the high level of quantum noise in the projection data will pass through to the final reconstructed volume. This motivates the development of denoising tools to effectively remove the noise, improve lesion conspicuity, and maintain image resolution.

In this work, a partial diffusion equation (PDE) based denoising technique was specifically developed for processing breast tomography data. This PDEtomo technique takes into account the noise distribution characteristic in the projection image after converting to the line integrals via the nonlinear logarithm operation.

Both the quantitative results in the simulation study and the visual inspection in human subject data study showed the promise of this new PDEtomo technique. In the simulation study, it was compared with Wiener technique, an adaptive technique that is accepted as a competitive denoising tool. The results show that the new denoising technique can achieve lower noise level in the reconstructed volume with higher resolution than Wiener technique. The low contrast lesion put in the center of the simulated breast can be better detected on the PDEtomo processed datasets than on the Wiener processed datasets, as is shown in Figure 4. Not only is the noise in the reconstructed slices filtered by PDEtomo lower than those by Wiener filtering, but the noise levels all over the breast region tend to be more uniform as well. This is shown in Figure 5. The advantage of PDEtomo over

Wiener filtering in terms of decreased noise level and improved noise uniformity are both
290 more evident for lower dose cases, which indicates that the PDEtomo technique holds
promise for processing datasets acquired at lower dose levels.

Even though the theoretical description of the noise variance in the projection image due
to the quantum noise and the logarithm operation is more approximate for the empirical
data, the PDEtomo technique still provides good denoised images.

295 There are some limitations in this study. Firstly, the simulated breast CT data are based
on a monochromatic x-ray beam with the kV value set to be approximately the same as
the effective kV value of the x-ray beam used to acquire the empirical data. Secondly, the
parameters in the measurement model used for adding noise to the simulated projection
images are all hypothetical, given that presently their empirical values are lacking. Hence,
300 the task of calibrating the dose in the simulation study cannot be fulfilled at this stage. In
future work, considerable optimization remains to be performed to calibrate the PDEtomo
technique using empirical images taken with physical phantoms as well as human
subjects. Given the robust trends shown in this study, however, the PDEtomo technique
should continue to match or outperform the Wiener technique, especially if dose is
305 further lowered such as to achieve a breast CT scan with equal or less dose than two-view
conventional mammograms.

Due to the very low photon fluence on each projection view in dedicated breast CT, the
electronic noise is one of the major sources of the overall noise, especially in dense breast
regions or if the dose is further reduced. The present version of the PDEtomo technique
310 doesn't consider the effects of additive electronic noise. It will be worthwhile to explore
the possibility of taking the characteristics of this type of noise into account in the

denoising technique or to combine it with a statistical-modeling approach that explicitly treats the electronic noise.

315 In conclusion, a partial diffusion equation based denoising technique was developed specifically for dedicated breast CT data. By incorporating into the algorithm the knowledge of the non-uniform distribution of the noise in the projection image after the preprocessing step, it provides excellent denoised data with sharp edges. The technique shows the most promise on datasets acquired with lower dose.

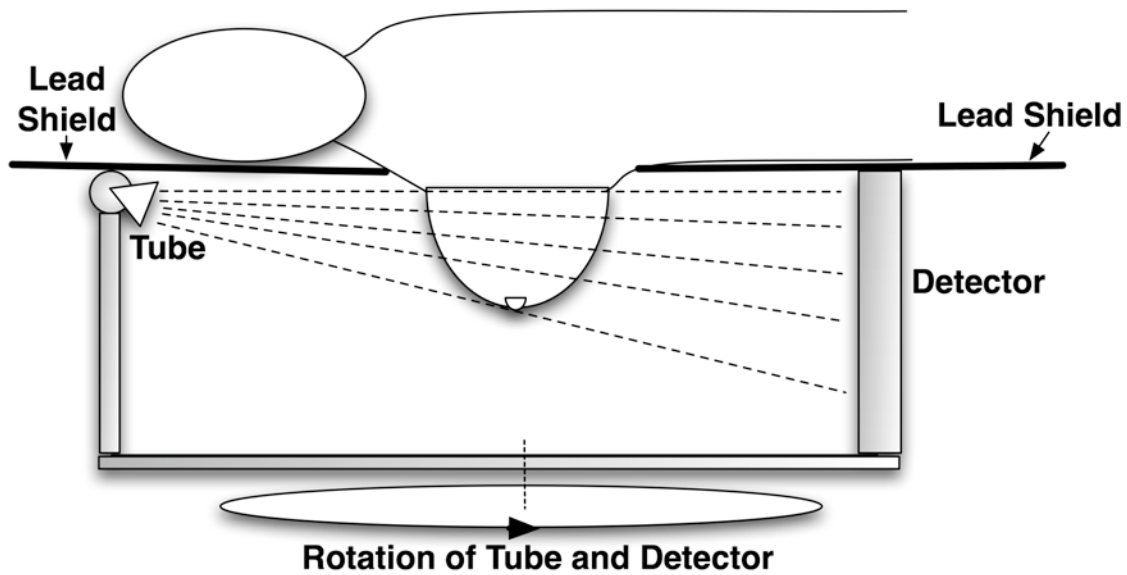
Acknowledgments

320

This work was supported in part by grants from the National Institutes of Health (R01 CA 94236 and R01 CA 112437) and the US Army Breast Cancer Research Program (W81XWH-05-1-0278).

List of Figures

| | | |
|-----|--|----|
| 325 | Figure 1 Illustration of a dedicated breast CT system. | 27 |
| | Figure 2 One-dimensional line integral profiles across the breast on a projection image. | 28 |
| | Figure 3 Illustration of the possible locations of image denoising module to be applied with respect to the reconstruction module for dedicated breast CT data. | 29 |
| 330 | Figure 4 The reconstructed slices of original, Wiener and PDEtomo processed datasets using the varying photon fluence levels from the simulation study..... | 30 |
| | Figure 5 (a) The reconstruction slices without a lesion. Along the horizontal lines marked in (a), local noise level profiles are computed for original, Wiener and PDEtomo processed datasets at I0 of (b) 2.5e3, (c) 5e3 and (d) 2.5e4. | 33 |
| 335 | Figure 6 CNR comparison between the original, Wiener denoised and PDE in a simulation study with I0=2.5e4..... | 34 |
| | Figure 7 (a) The target reconstruction around a high contrast object from original, Wiener processed and PDEtomo processed datasets, and (b) noise-resolution plot with I0=2.5e4..... | 36 |
| | Figure 8 Human Subject Result No.1 | 37 |
| 340 | Figure 9 Human Subject Result No.2 | 38 |



345 **Figure 1 Illustration of a dedicated breast CT system.**
The x-ray tube and flat-panel detector rotate together around the breast. And the breast is the only region to be illuminated.

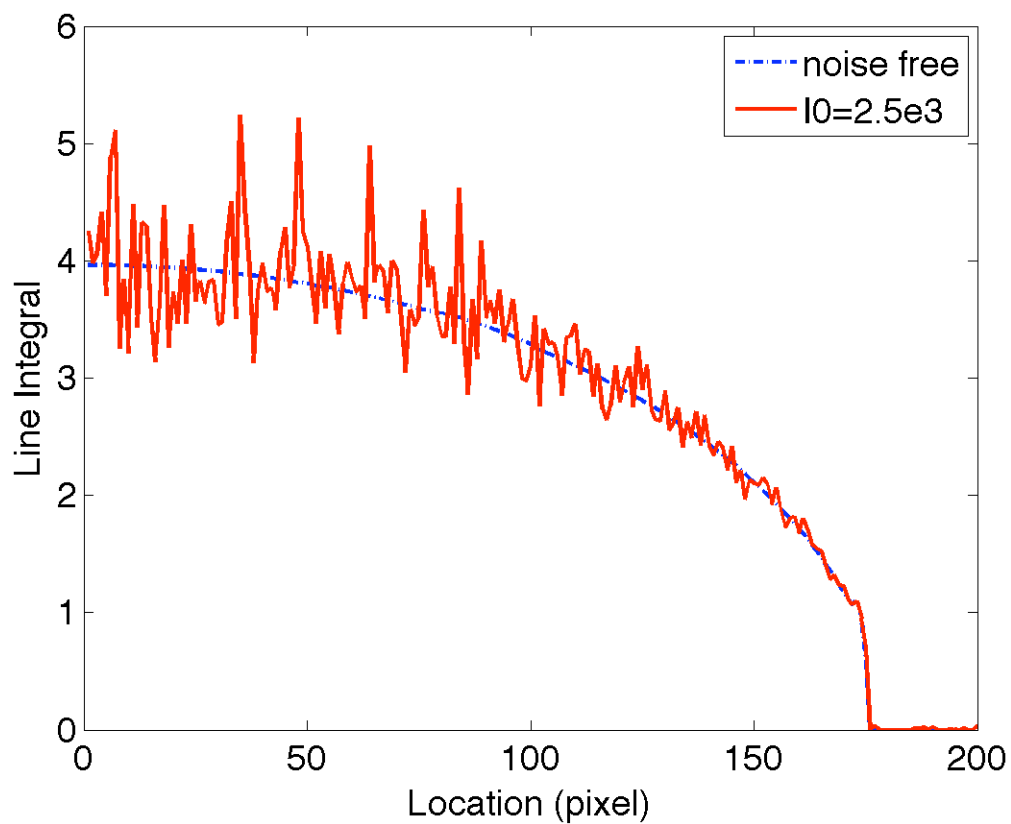
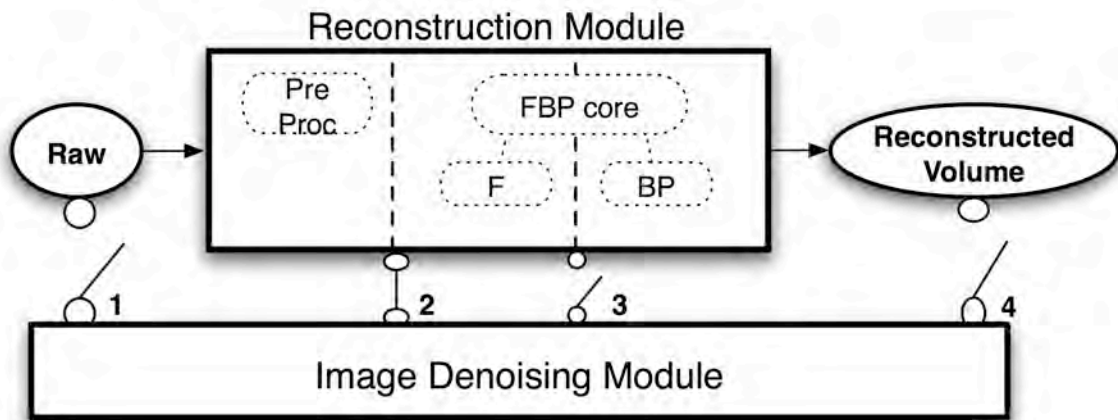


Figure 2 One-dimensional line integral profiles across the breast on a projection image.

The dashed (blue) and continuous (red) plots correspond to noise free case and the case with $I_0=2.5e3$, respectively. The variance of line integral is larger at the center of breast region, and gets lower toward the skin.



355

Figure 3 Illustration of the possible locations of image denoising module to be applied with respect to the reconstruction module for dedicated breast CT data.

In this study, the denoising techniques are applied at location 2.

360

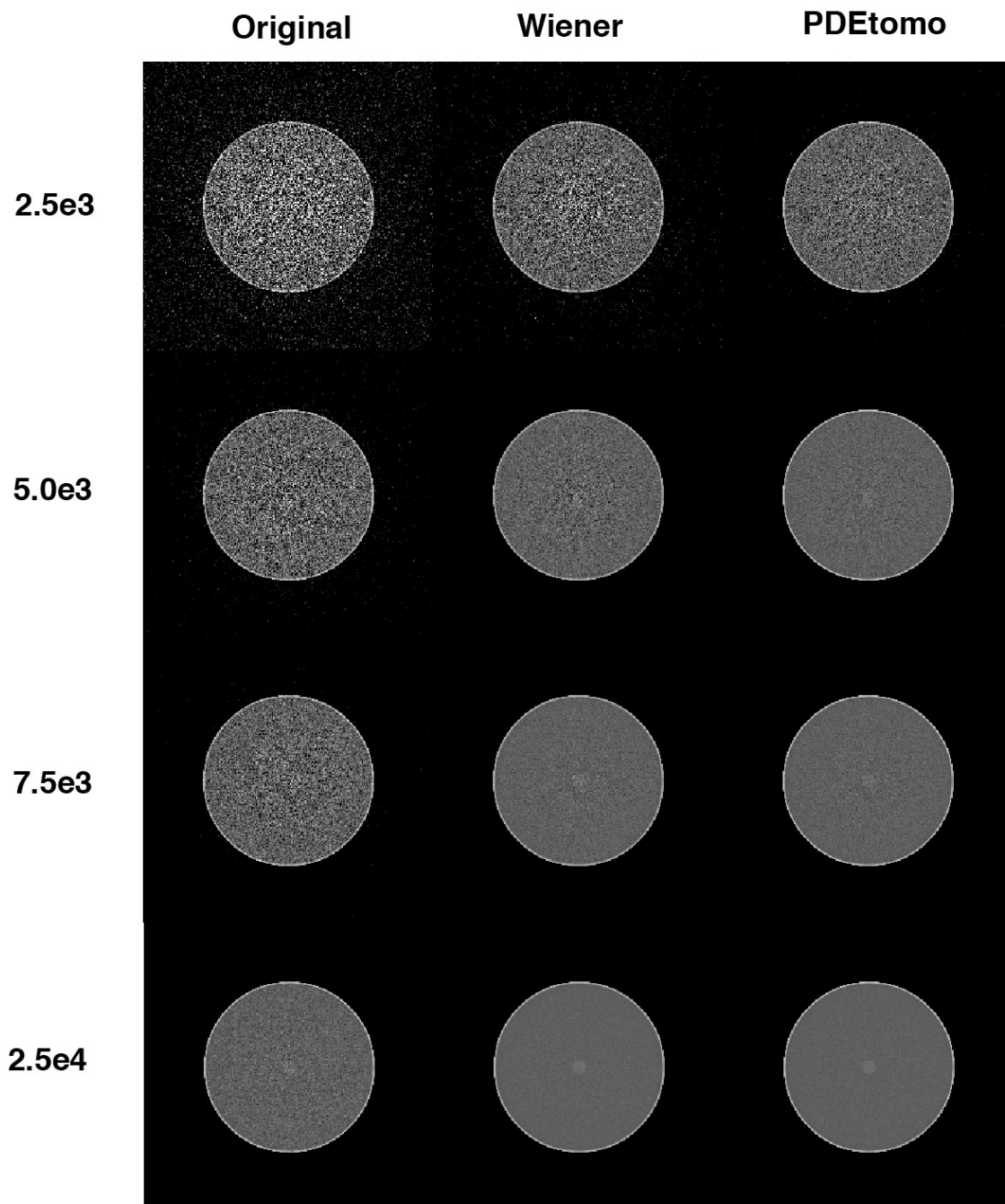


Figure 4 The reconstructed slices of original, Wiener and PDEtomo processed datasets using the varying photon fluence levels from the simulation study.

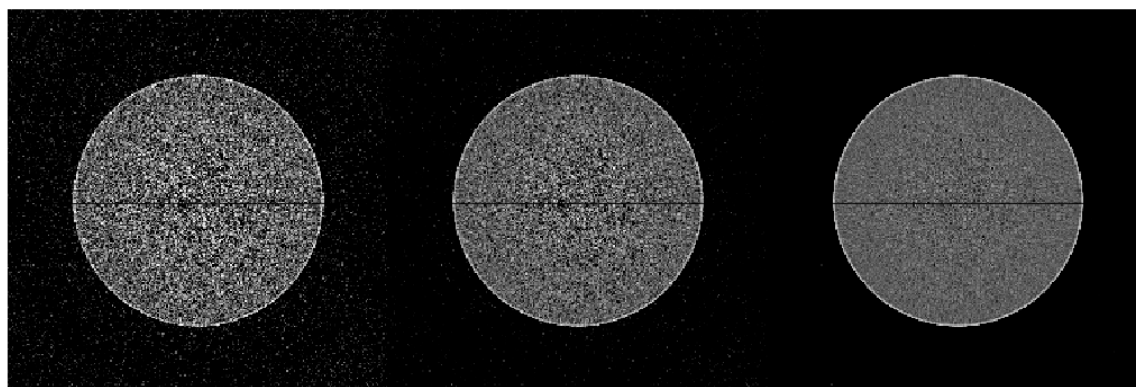
The central low contrast lesion is visible only at the highest fluence level with the original dataset. It is visible at the highest two fluence levels with the Wiener processed dataset, whereas it is visible at the highest three fluence levels with the PDEtomo technique.

(a)

Original

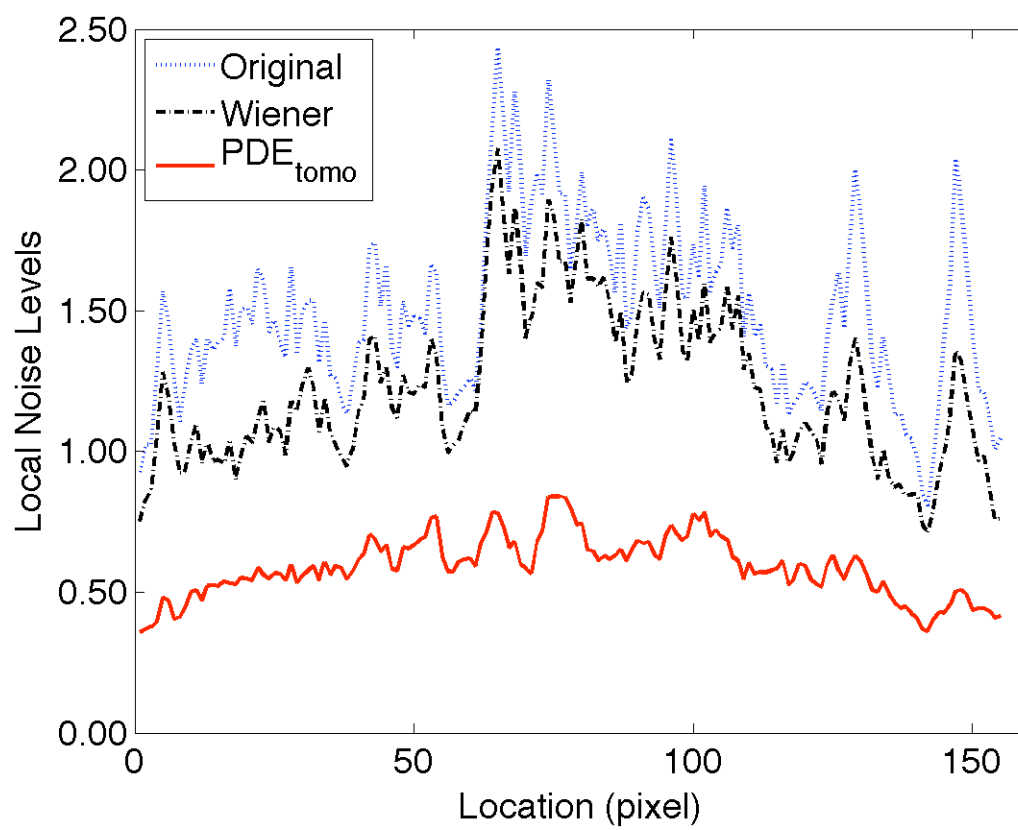
Wiener

PDEtomo

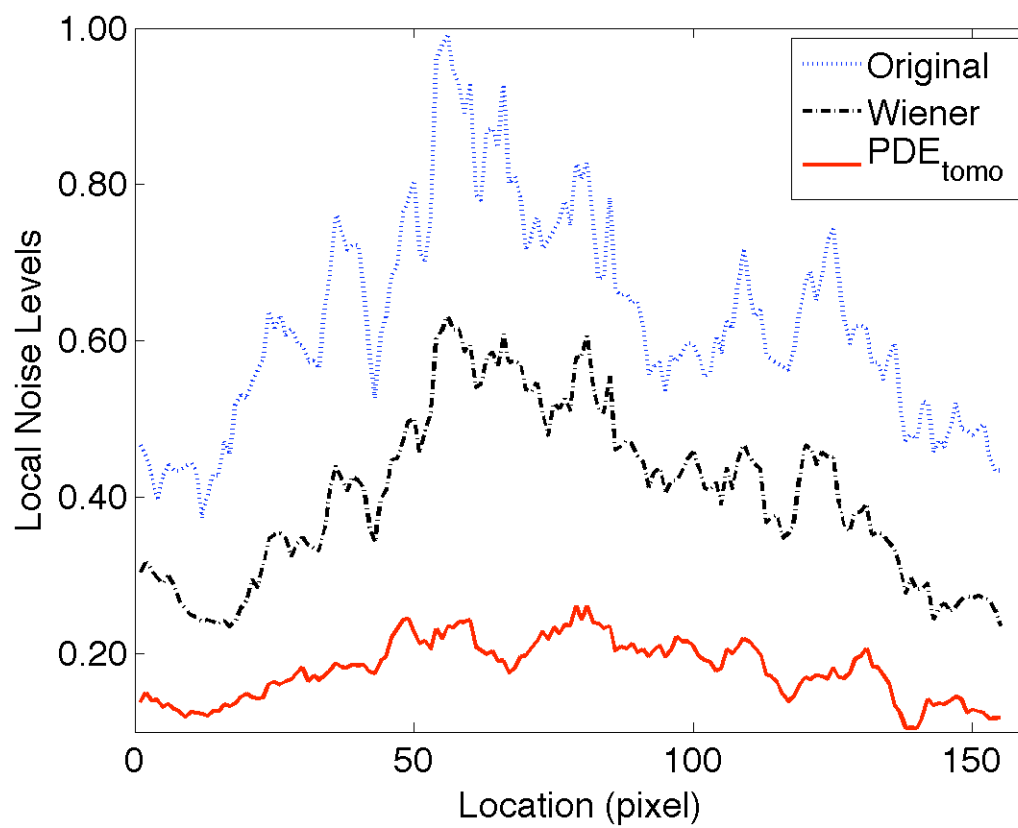


370

(b)



(c)



375 (d)

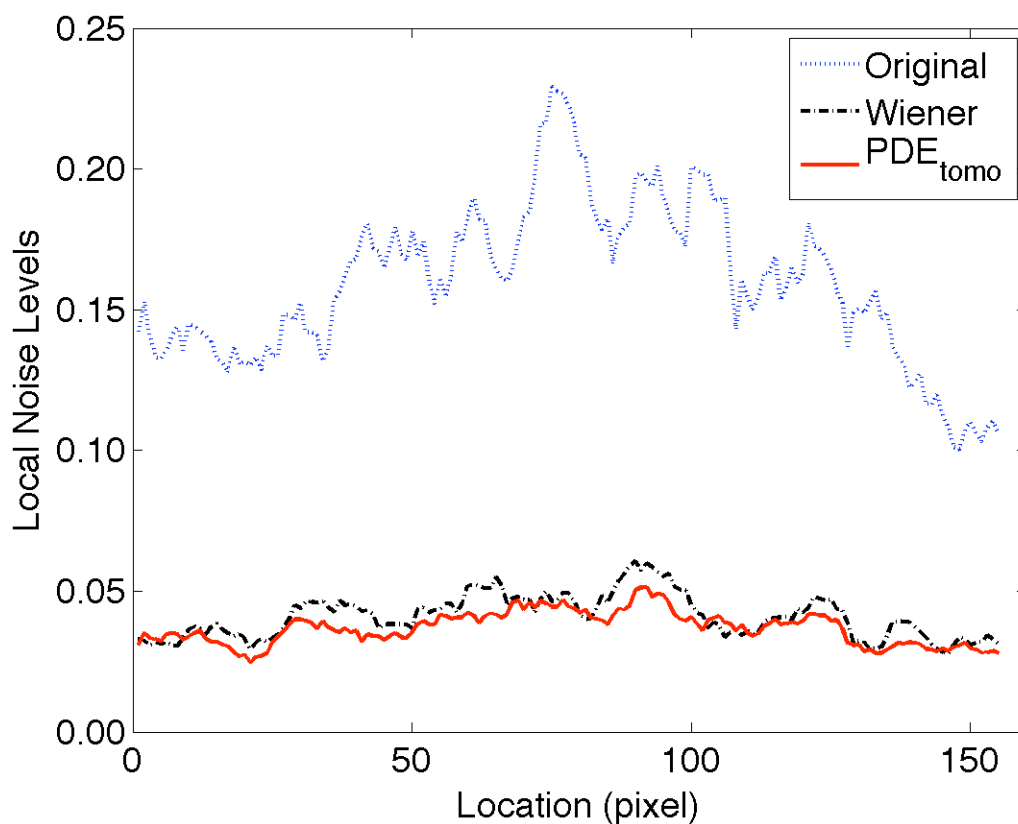
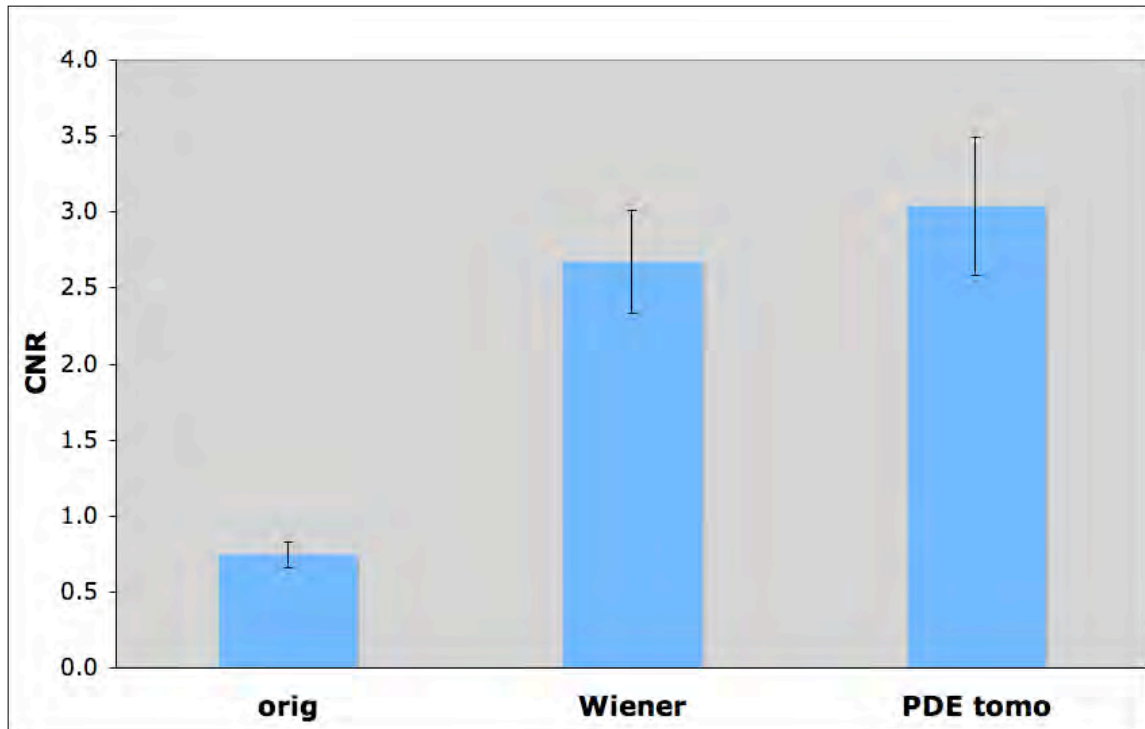


Figure 5 (a) The reconstruction slices without a lesion. Along the horizontal lines marked in (a), local noise level profiles are computed for original, Wiener and PDE_{tomo} processed datasets at I0 of (b) 2.5e3, (c) 5e3 and (d) 2.5e4.

380 **PDE_{tomo} processed results have lower and more uniform local noise levels than Wiener results. The difference is more manifest at lower fluence level.**

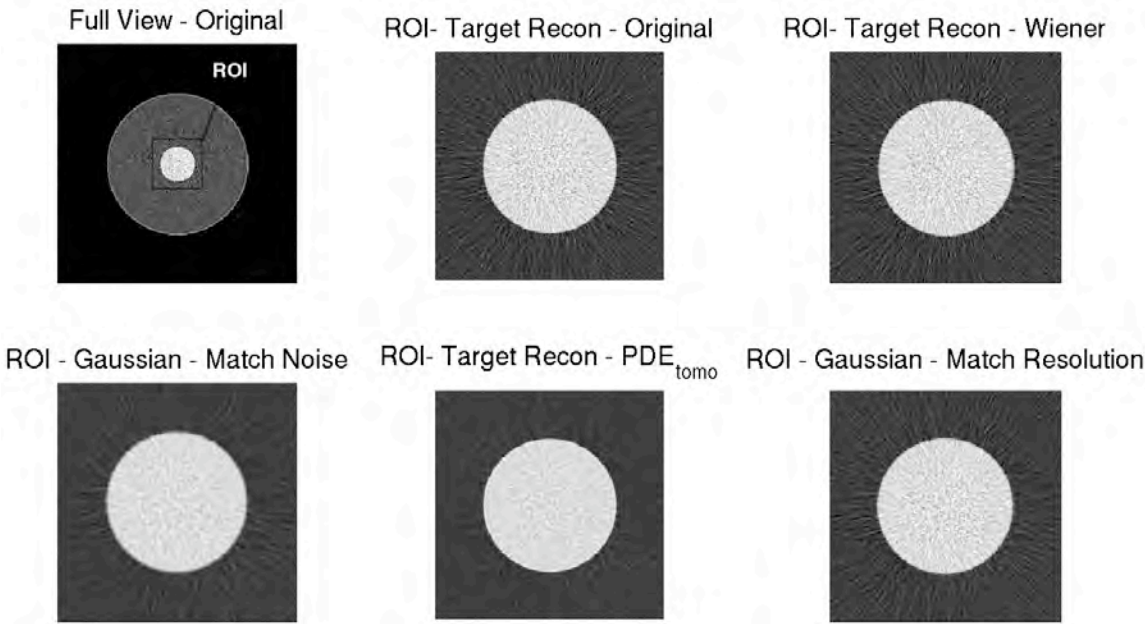


385 **Figure 6 CNR comparison between the original, Wiener denoised and PDE in a**
simulation study with $I_0=2.5e4$.

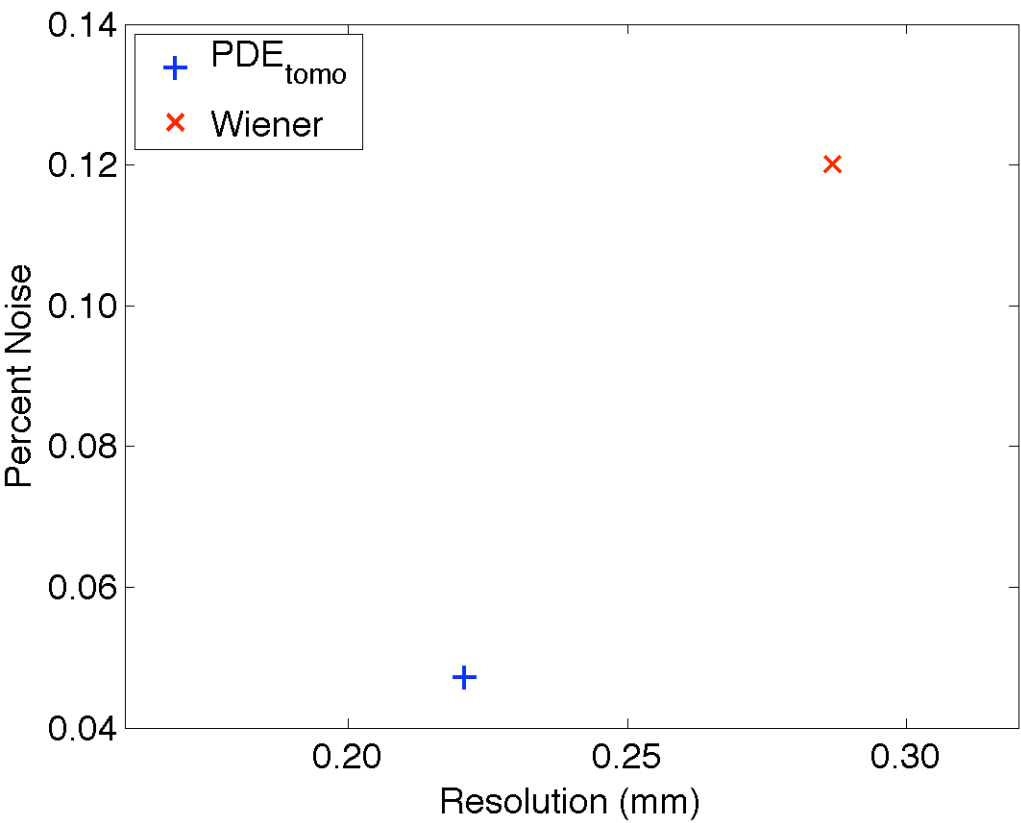
The PDEtomo has consistently higher CNRs than Wiener for the same data. The paired two-tailed student t test gives a p-value of 0.0036, which indicate the difference between the CNRs of PDEtomo and Wiener are statistically significant.

390

(a)

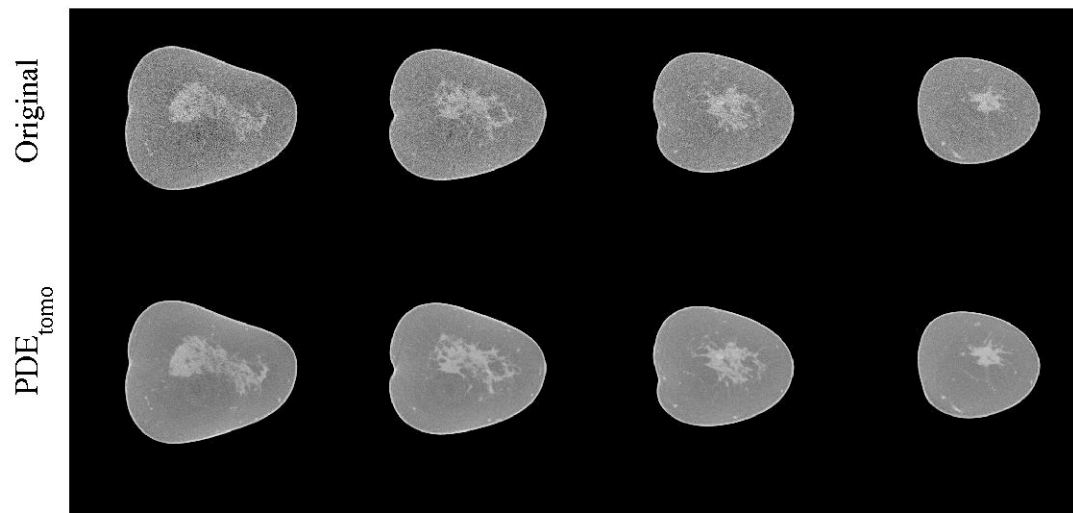


(b)



395 **Figure 7 (a) The target reconstruction around a high contrast object from original, Wiener processed and PDEtomo processed datasets, and (b) noise-resolution plot with $I_0=2.5e4$.**

The data processed by PDEtomo has a lower noise level and higher resolution than the one processed by Wiener. The two Gaussian kernel blurred ones are to match
400 **the noise level or the resolution with the PDEtomo processed data.**



405 **Figure 8 Human Subject Result No.1**

Top row shows original reconstruction, coronal slices from normal breast. Bottom row shows same slices with PDE_{tomo} denoising, resulting in remarkably reduced noise levels.

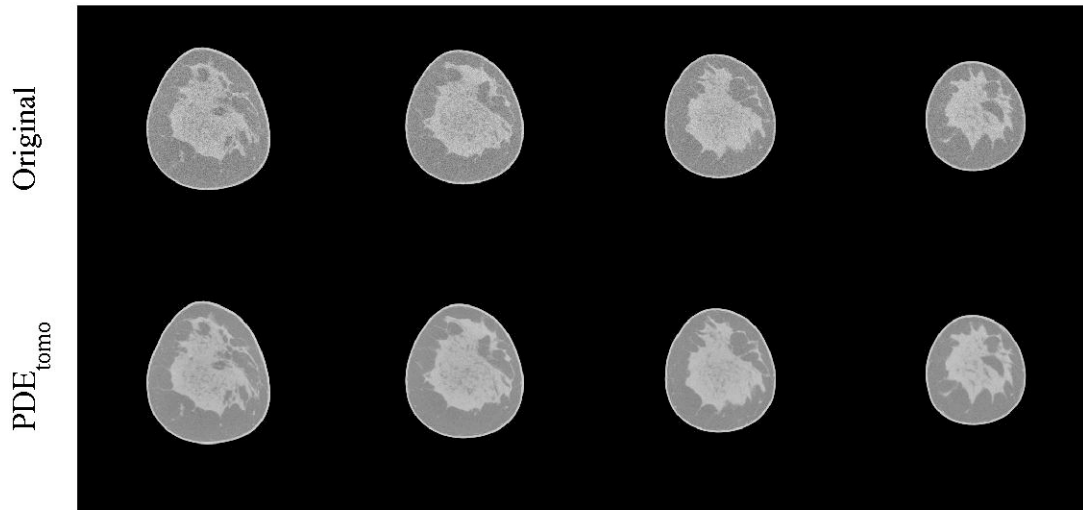


Figure 9 Human Subject Result No.2

Top row shows original reconstruction, coronal slices from normal breast. Bottom row shows same slices with PDE_{tomo} denoising, resulting in markedly reduced noise levels.

Reference

1. ACS, "American Cancer Society: Cancer Facts and Figures 2007," Atlanta, GA: American Cancer Society (2007).
- 420 2. S. W. Fletcher and J. G. Elmore, "Mammographic screening for breast cancer," New England Journal of Medicine 348, 1672-1680 (2003).
3. L. Nystrom, I. Andersson, N. Bjurstam, J. Frisell, B. Nordenskjold and L. E. Rutqvist, "Long-term effects of mammography screening: updated overview of the Swedish randomised trials," Lancet 359, 909-919 (2002).
- 425 4. R. H. VP Jackson, S.A. Feig, D.B. Kopans, "Imaging of the radiographically dense breast," Radiology 188, 297-301 (1993).
5. L. T. Niklason, B. T. Christian, L. E. Niklason, D. B. Kopans and et al., "Digital tomosynthesis in breast imaging," Radiology 205, 399-406 (1997).
6. J. Dobbins and D. Godfrey, "Digital x-ray tomosynthesis: current state of the art and clinical potential," Physics in Medicine and Biology 48, R65-R106
430 (2003).
7. J.M. Boone, T.R. Nelson, K.K. Lindfors, et al., "Dedicated breast CT: radiation dose and image quality evaluation," Radiology 221, 657-667 (2001).
8. J.M. Boone, N. Shah, T.R. Nelson, "A comprehensive analysis of DgN(CT) coefficients for pendant-geometry cone-beam breast computed tomography,"
435 Medical Physics 31, 226-235 (2004).
9. X. Gong, A. A. Vedula and S. J. Glick, "Microcalcification detection using cone-beam CT mammography with a flat-panel imager," Physics in Medicine and Biology 49, 2183-2195 (2004).
10. C. J. Lai, C. C. Shaw, M. C. Altunbas, Y. Meng, et al., "Effects of radiation dose level on calcification visibility in cone beam breast CT: a preliminary study," Proceedings of SPIE 6142, 614233-1:614233-8 (2006).
440
11. R. Ning, "Flat panel detector-based cone beam volume CT imaging," Medical Physics 30, 1370-1370 (2003).
12. R. L. McKinley, M. P. Tornai, E. Samei and M. L. Bradshaw, "Simulation Study of a Quasi-monochromatic Beam for X-ray Computed Mammothomography," Medical Physics 31, 800-813 (2004).
445
13. C. H. Chang, J. L. Sibala, S. L. Fritz, J. H. Gallagher, S. J. Dwyer and A. W. Templeton, "Computed tomographic evaluation of breast," American Journal of Roentgenology 131, 459-464 (1978).
- 450 14. J.M. Boone, A.L.C. Kwan, T.R. Nelson, N. Shah, et al., "Performance assessment of a pendant-geometry CT scanner for breast cancer detection," Proceedings of SPIE 5145, 319-323 (2005).

15. P. J. La Riviere, "Penalized-likelihood sinogram smoothing for low-dose CT," *medical Physics* 32, 1676-1683 (2005).
- 455 16. J. Wang, T. F. Li, H. B. Lu and Z. R. Liang, "Penalized weighted least-squares approach to sinogram noise reduction and image reconstruction for low-dose X-ray computed tomography," *IEEE Transactions on Medical Imaging* 25, 1272-1283 (2006).
- 460 17. J. M. Zhong, R. L. Ning and D. Conover, "Image denoising based on multiscale singularity detection for cone beam CT breast imaging," *IEEE Transactions on Medical Imaging* 23, 696-703 (2004).
18. P. Perona and J. Malik, "Scale-space and edge detection using anisotropic diffusion," *IEEE Transactions on Pattern Analysis and Machine Intelligence* 12, 629-639 (1990).
- 465 19. J. Weichert, *Anisotropic diffusion in image processing* (Tuebner: Stuttgart, 1998).
20. T. L. Pope, M. E. Read, T. Medsker, A. J. Buschi and A. N. Brenbridge, "Breast skin thickness - normal range and causes of thickening shown on film-screen mammography," *Journal Of The Canadian Association Of Radiologists-Journal De L Association Canadienne Des Radiologistes* 35, 365-368 (1984).
- 470 21. J. Hsieh, "Adaptive streak artifact reduction in computed tomography resulting from excessive X ray photon noise," *Medical Physics* 25, 2139-2147 (1998).
- 475 22. L. A. Feldkamp and J. W. Kress, "Practical cone-beam algorithm," *Journal of Optical Society of America, A* 1, 612-619 (1984).
23. D. A. McQuarrie, *Mathematical methods for scientists and engineers* (University Science Books, 2003).
- 480 24. J. M. Boone, "Breast CT: Its prospect for breast cancer screening and diagnosis.," In: A. Karellas, M.L. Giger, eds. 2004 Syllabus: Advances in Breast Imaging Physics, Technology, and Clinical Applications. Oak Park, ILL: Radiological Society of North America 165-177 (2004).
25. J. T. Bushberg, J. A. Seibert, E. M. Leidholdt Jr. and J. M. Boone, *The essential physics of medical imaging* (Lippincott Williams & Wilkins, 2001).
- 485 26. R. Ning, B. Chen, D. Conover, et al., "Flat panel detector-based cone beam volume CT breast imaging: Phantom study," *Radiology* 221, 544-544 (2001).
27. B. Chen, R. Ning, "Cone-beam volume CT breast imaging: Feasibility study," *Medical Physics* 29, 755-770 (2002).

On the Development of a Gaussian Noise Model for Scatter Compensation

Jessie Q. Xia^{1,3}, Georgia D. Tourassi^{1,2}, Joseph Y. Lo^{1,2,3}, and Carey E. Floyd, Jr.^{1,2,3}

¹Duke Advanced Imaging Laboratories, Department of Radiology,

²Medical Physics Graduate Program, Department of Radiology,
Duke University Medical Center, Durham, NC 27710;

³Department of Biomedical Engineering, Duke University, Durham, NC 27708

ABSTRACT

The underlying mechanism in projection radiography as well as in computed tomography (CT) is the accumulative attenuation of a pencil x-ray beam along a straight line. However, when a portion of photons is deviated from their original path by scattering, it is not valid to assume that these photons are the survival photons along the lines connecting the x-ray source and the individual locations where they are detected. Since these photons do not carry the correct spatial information, the final image is contaminated. Researchers are seeking techniques to reduce scattering, and hence, improve image quality, by scatter compensation. Previously, we presented a post-acquisition scatter compensation technique based on an underlying statistical model. We used the Poisson noise model, which assumed that the signals in the detector individually followed the Poisson process. Since most x-ray detectors are energy integrating rather than photon counting, the Poisson noise model can be improved by taking this property into account. In this study, we developed a Gaussian noise model by the matching-of-the-first-two-moments method. The Maximum Likelihood Estimator of the scatter-free image was derived via the expectation maximization (EM) technique. The maximum a posteriori estimate was also calculated. The Gaussian noise model was preliminarily evaluated on a full-field digital mammography system.

KEYWORDS: Scatter Compensation, Scatter Reduction, Gaussian Noise Model, Expectation Maximization

1. INTRODUCTION

Scattered radiation degrades medical images. A recent Monte Carlo study showed that scattered radiation causes the drop of low-frequency modulation transfer function (MTF), changes the shape of MTF and adds considerable noise to projection images¹. In computed tomography (CT), scattered radiation leads to cupping artifacts on reconstructed sections. Therefore, removal of scattered radiation from projection images is essential for improved image quality, particularly for the latest advanced imaging radiography techniques including dedicated breast CT and breast tomosynthesis, which typically do not use anti-scatter grids.

There are two categories of scatter compensation techniques: hardware based ones and numerical compensation methods. This study uses a numerical compensation method to develop a statistical scatter reduction technique. Previously, the exposure value of each pixel recorded by a detector was modeled by Poisson distribution². For flat-panel detectors, which belong to the type of energy integrating rather than photon counting, the underlying statistics is a compound Poisson process³. It may be well approximated by Gaussian distribution.

In this study, we will propose a Gaussian noise model for scatter reduction, and derive a maximum likelihood expectation maximization (MLE or MLEM) algorithm and a maximum a posteriori (MAP) algorithm. We will then apply the algorithms to radiographs acquired on FFDM for preliminary evaluation.

2. MATERIALS AND METHODS

2.1 Gaussian Noise Model

In the chosen numerical scatter compensation scheme, the projection image is the sum of the primary radiation and scattered radiation. We have modeled scattered radiation as the two-dimensional convolution of primary radiation with a scatter kernel, which is displayed as a double exponential function (Figure 1).

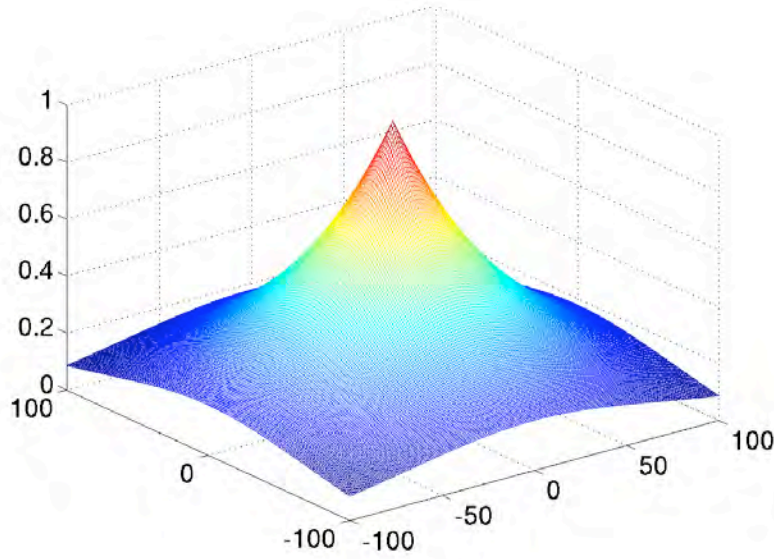


Figure 1: Schematic of a scatter kernel with a radically exponential shape. It has two parameters: full width at half maximum and magnitude).

By the matching-of-the-first-two-moments method, we approximated the energy-integrating signal by using a Gaussian distribution and created a scatter compensation model called the Gaussian noise model.

$$\begin{aligned} d_i | B, \sigma_{i1}^2 &\sim \text{Gaussian}(b_i, \sigma_{i1}^2) \\ s_i | B, \sigma_{i2}^2 &\sim \text{Gaussian}((B ** P)_i, \sigma_{i2}^2) \\ y_i = d_i + s_i | B, \sigma_{i1}^2, \sigma_{i2}^2 &\sim \text{Gaussian}(b_i + (B ** P)_i, \sigma_{i1}^2 + \sigma_{i2}^2) \end{aligned} \tag{1}$$

where d_i , s_i , and y_i are pixel values at location i corresponding to primary, scattered and total radiation, respectively, b_i is the expectation of d_i , and σ_{i1}^2 and σ_{i2}^2 are the variance of pixel values related to the primary radiation and scattered radiation, respectively.

Using the expectation maximization (EM) algorithm shown in the appendix, the MLE of the ideal scatter-free image was derived with analytical form shown in Equation (2).

$$\begin{aligned} b_k^{(n+1)} &= b_k^{(n)} + w_k \cdot [y_k - (b_k^{(n)} + (B^{(n)} ** P)_k)], \\ w_k &= \sigma_{k1}^2 / (\sigma_{k1}^2 + \sigma_{k2}^2) \end{aligned} \quad (2)$$

MLE estimate is known to increase high frequency image noise. To overcome this, some constraints can be put on the noise level within the estimated B , in other words, prior information about B can be provided. Thus, by Bayes's Rule,

$$p(B|Y) \propto p(Y|B)p(B), \quad (3)$$

where $p(B|Y)$ is the posterior joint distribution of B , given the measured pixel values $Y = \{y_i; i=1, \dots, N\}$, $p(Y|B)$ is equal to the likelihood of B , and $p(B)$ is the prior joint distribution of $B = \{b_i; i=1, \dots, N\}$.

We assumed B is a Markov random process. It therefore follows a Gibbs distribution:

$$p(B) = \frac{1}{K} e^{-U(B)/\beta}, \quad (4)$$

where K is a normalizing factor which is independent of B , $U(B)$ is the energy function, and β is a free parameter adjusting the relative weight of this prior on the maximum *a posteriori* estimator of B . When β approaches infinity, the MAP of B approaches the MLE of B .

The energy function is the sum of the potential function, i.e.,

$$U(B) = \sum_{c \in C} V_c(B), \quad (5)$$

where C is the set comprised of all cliques in the image. In this study, the Gibbs prior is defined over a second-order neighborhood system (for each pixel, its north, south, east, and west neighboring pixels plus its four diagonal neighboring pixels), with each clique comprised of two neighboring pixels. There are many forms of the potential function $V_c(B)$. We chose one that is adaptive to discontinuity⁴:

$$V_c(\{b_i : b_j\}) = \frac{(b_i - b_j)^2}{\delta_c^2 + (b_i - b_j)^2}, \quad (6)$$

where i and j are the neighboring pixels within the clique $i \sim j$ and b_i and b_j represent their respective intensities. δ_c is an adjustable parameter to regulate the cut-off frequency of the noise in the image.

The MAP estimate of $\{b_i\}$ was calculated through the two-step maximization procedure proposed by Hebert and Leahy⁵.

2.2 Test Images

Images were acquired with a Siemens prototype digital mammography system (Mammomat Novation^{DR}; Siemens, Erlangen, Germany) with 70 μm isotropic resolution. Uniform breast phantoms (CIRS, Inc., Norfolk, VA) were imaged (28kVp), with a Mo/Mo target/filter

combination. The phantoms were designed to be radiographically equivalent to a 4-cm-thick compressed breast with 50% glandular tissue density. A built-in square-shaped dent in the center of the phantom mimicked a high-contrast lesion in the digital mammography images. All images were acquired without an anti-scatter grid. For the purpose of scatter measurement, all images were repeated with an array of beam stops (lead discs 3 mm in diameter) superimposed on the breast phantoms. Because lead discs absorb all the primary radiation, only scatter radiation can be detected behind them (Figure 2).

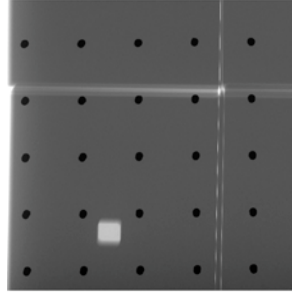


Figure 2: Radiograph of the tissue equivalent slabs. The arrays of black disks are the shadow of beam stops. The CNR values are obtained based on the bright square region of interest.

Images were then be fed into the algorithms for processing. The results were then evaluated through various metrics described in the following subsection.

2.3 Image Evaluation Metrics

Three algorithms were employed to estimate the expected amount of primary radiation. Its effect was measured by the residual scatter fraction (RSF). At the same time, we anticipated that the contrast-to-noise ratio (CNR) would be constrained or even improved after image processing. We implemented a metric to estimate post-contrast CNR. Finally, we monitored with a test bar the effect of the algorithms on the spatial resolution of the images.

2.3.1 Residual Scatter Fraction

Scatter fraction (SF) is defined as the ratio of scatter radiation to total radiation. Residual scatter fraction (RSF) indicates how much of the scatter radiation remains after applying the scatter compensation algorithm.

For our imaging technique, two sets of images of the phantom were obtained: one with, and one without, a beam stop array. The signals behind beam stops (lead discs) comprise the scatter radiation, while the total radiation, which is the sum of primary radiation and scatter radiation, will reach the region without beam stops. We calculated the measured primary radiation (P_{measured}) by subtracting the mean radiation of a region-of-interest (ROI) behind a beam stop from the mean of the same ROI location without a beam stop. In the image processed for scatter compensation, the mean of total radiation (T) in the same ROI location ($T_{\text{estimated}}$) is the sum of the residual scatter radiation and the primary radiation. Thus,

$$RSF = \frac{T_{\text{estimated}} - P_{\text{measured}}}{T_{\text{estimated}}} . \quad (7)$$

2.3.2 Contrast, Noise and CNR

Contrast was defined as the ratio of the difference between the mean radiation value of the lesion (T_{lesion}) and the background ($T_{\text{background}}$) to the mean of the background, that is,

$$\text{Contrast} = \frac{T_{\text{lesion}} - T_{\text{background}}}{T_{\text{background}}} . \quad (8)$$

Noise was derived by dividing the standard deviation ($STD_{\text{background}}$) by the mean of the background radiation ($T_{\text{background}}$):

$$\text{Noise} = \frac{STD_{\text{background}}}{T_{\text{background}}} . \quad (9)$$

CNR is the ratio of the contrast to the noise, i.e.,

$$\text{CNR} = \frac{\text{Contrast}}{\text{Noise}} = \frac{T_{\text{lesion}} - T_{\text{background}}}{STD_{\text{background}}} . \quad (10)$$

2.3.3 Resolution

Due to the nonlinearity of the resolution algorithm, we could not use metrics like MTF, which are designed for a linear system. Instead, a test bar, comprised of alternating bright and dark lines with sizes corresponding to Nyquist frequencies with square wave function, was embedded in the phantom image.

The contrast improvement factor (CIF), defined as the ratio of the contrast after image processing to the initial contrast, was obtained for the test bar with various initial contrast settings. A CIF of 1 or greater was used as the criterion for retaining the spatial resolution. The minimal initial contrast that the test bar can allow with CIF of 1 or greater was recorded as an indication of the effect of the image processing on resolution. For the various initial contrasts, the corresponding CIF was computed arbitrarily at iteration 16. We determined the minimal initial contrast value that has a CIF of 1 or greater.

3. RESULTS

3.1 Scatter Compensation Technique -- Tissue Equivalent Slabs

Figure 3 and Table 1 give the RSF, CNR and resolution results for MLE and MAP algorithms based on a Poisson noise model and Gaussian noise model. Both MLE algorithms reduced RSF values to close to zero and decreased CNR values from the original unprocessed value of 47 to slightly below 40. The minimal contrast that is retainable during processing using our Poisson-model-based MAP algorithm was 1.8%. The MAP algorithms were as equally effective as their MLE counterparts in removing scattered radiation from the radiograph; however, they increased the CNR values to 56 and 63, for the Poisson noise model and Gaussian model, respectively. The minimal contrast retainable using the Gaussian model based MAP algorithm was 2.0%, slightly higher than that of Poisson-model-based MAP (1.8%).

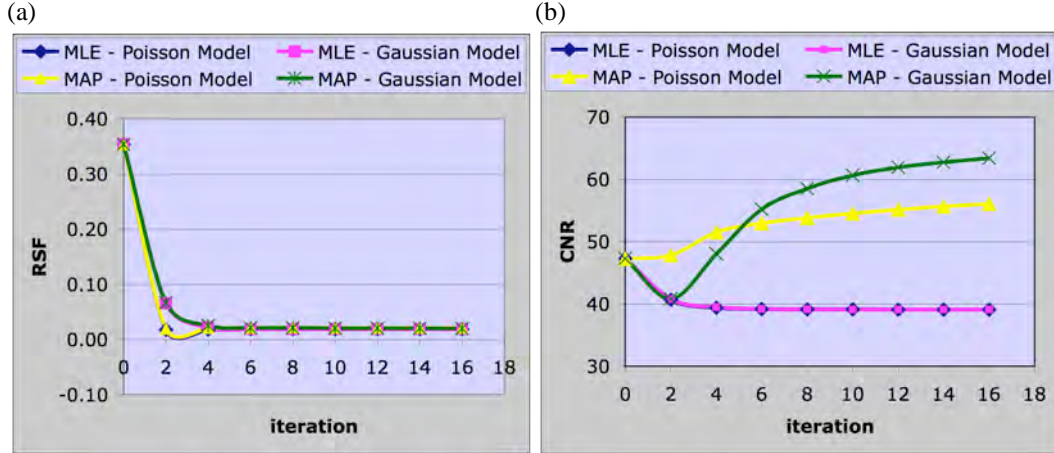


Figure 3: Plots of (a) residual scatter fraction and (b) contrast to noise ratio as the function of iteration numbers between MLE and MAP estimates of scatter free image $\{b_i\}$ based on Poisson and Gaussian noise models. While both techniques were effective at removing scattered radiation, the MAP based on the Gaussian noise model showed greater CNR improvement.

Table 1: Resolution results of MAP estimates based on Poisson noise model and Gaussian noise model with the magnitude of scatter kernel of 0.52. The resolution results from the two models are close to each other.

| | Poisson Noise Model | Gaussian Noise Model |
|---|---------------------|----------------------|
| Minimum initial contrast that is retainable during processing | 1.8% | 2.0% |

How the magnitude of the scatter kernel impacted the MAP algorithm based on the Gaussian noise model was also investigated. Figure 4(a) shows the RSF as a function of iteration for different magnitudes. When the magnitude is zero, there is no scatter reduction effect. As the magnitude increases, the steady-state RSF decreases. When the magnitude is larger than the measured value of 0.52, the scattered radiation is overcompensated such that RSF is less than zero. Figure 4(b) depicts CNR results for the same scatter kernel magnitudes. Overall, the larger the magnitude, the less CNR will increase. In the case of resolution, the smaller the magnitude, the lower the resolution (Table 2). For the magnitude of 0.2, the minimal contrast retainable during processing was 2.7%. For the magnitude of 0, where there was no scatter compensation, no contrast was retainable during processing.

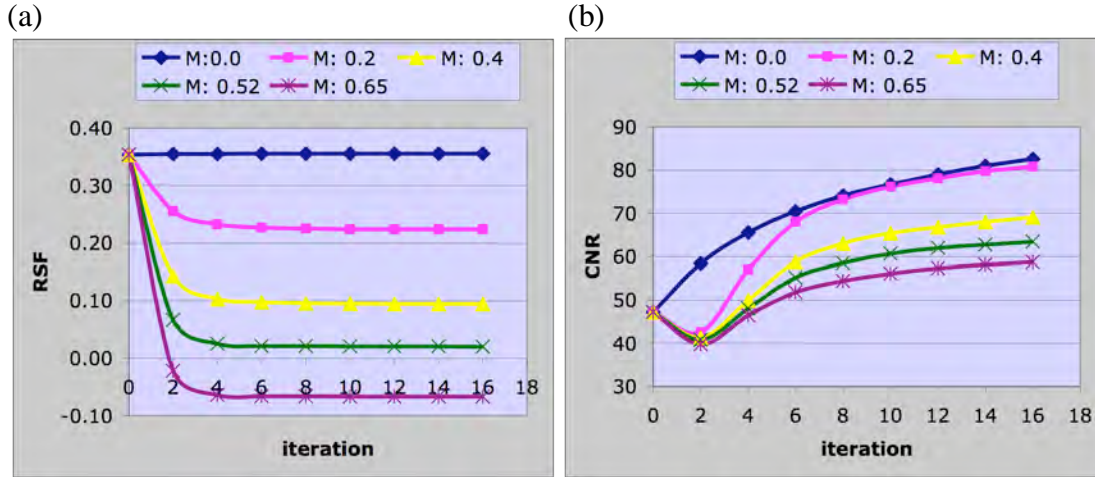


Figure 4: Plots of (a) residual scatter fraction and (b) contrast to noise ratio as the function of iteration numbers were shown for various magnitudes of scatter kernel using MAP estimates of scatter free image $\{b_i\}$ based on the Gaussian noise model. A magnitude of 0.0 corresponds to no scatter removal, whereas a magnitude of 0.65 overcompensates the scattered radiation, resulting in negative residual scatter fraction values. At each magnitude level, the contrast increases asymptotically..

Table 2: Resolution results of the Gaussian noise model based MAP estimates with various magnitudes of scatter kernel. The larger the magnitude of scatter kernel, the sharper the processed image is. For the magnitude of zero, i.e., no scatter removal, the resolution is always degraded.

| Magnitude | 0.0 | 0.2 | 0.4 | 0.52 | 0.65 |
|--------------------------|-----|------|------|------|------|
| Minimal initial contrast | --- | 2.7% | 2.2% | 2.0% | 2.0% |

3.2 Scatter Compensation Technique -- Anthropomorphic Phantom

The scatter removal procedure reduced SF of the radiograph acquired without a grid from 45% to 10%, the level that an anti-scatter grid achieves (Figure 5, Table 3). At the same time, the procedure improved the CNR to around twice the value on the image acquired with a grid.

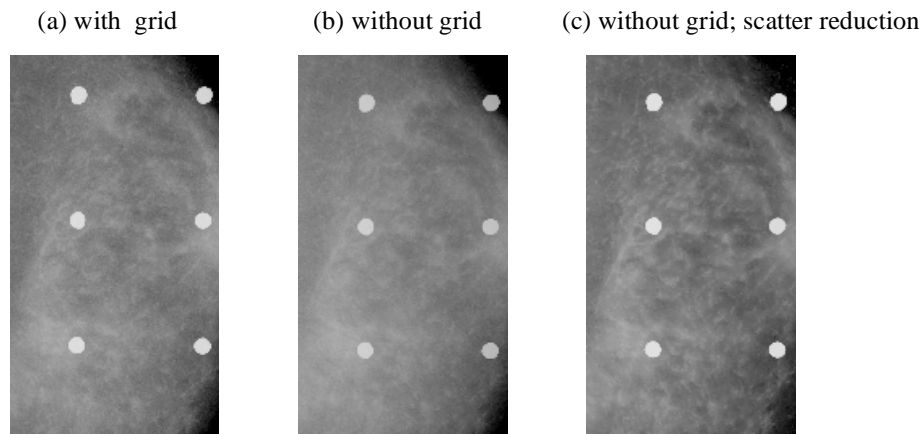


Figure 5: Radiographs of the breast anthropomorphic phantom, (a) with an anti-scatter grid, (b) without an anti-scatter grid, and (c) without an anti-scatter grid and with scatter reduction.

Table 3: Corresponding residual scatter fraction and contrast to noise ratio results for the three images shown in Figure 5.

| | With grid | w/o grid | w/o grid; scatter reduction |
|------------|-----------|----------|-----------------------------|
| RSF | 11% | 45% | 10% |
| CNR | 7.04 | 6.99 | 15.29 |

4. DISCUSSION

In this study, both MLE and MAP estimates of the scatter free image were derived based on a novel Gaussian noise model for energy-integrating detectors. The preliminary results were obtained on the two types of phantoms (tissue equivalent slabs and a breast anthropomorphic phantom) obtained on a full-field digital mammography system. Both MLE and MAP techniques were effective in removing the scattered radiation, though MAP outperformed MLE in CNR. For the specific phantom and imaging condition, the MAP of the Gaussian noise model outperformed the MAP of the Poisson noise model.

The next phase of this research will include a comprehensive evaluation of the scatter reduction technique on images acquired on a FFDM system. Also the technique can be applied on dedicated breast CT data for scatter reduction.

5. ACKNOWLEDGMENTS

The authors wish to thank Professor Michael Lavine in Institute of Statistics and Decision Science (ISDS) of Duke University for useful discussions.

This work was partially supported in part by USAMRMC W81XWH-05-1-0278, NIH R01-CA94236, and NIH R01-CA112337.

6. APPENDIX

Derivation of MLE Algorithm based on Gaussian Noise Model

Due to the convolution operation, the estimation of $B = \{b_i; i=1 \dots N\}$ directly from Y does not have a simple analytic form. The MLE of B is thus derived through the EM algorithm as follows.

Treat the measured $Y = \{y_i, i=1, \dots, N\}$ as an incomplete dataset, and unobserved $(D, S) = \{(d_i, s_i), i=1, \dots, N\}$ as a complete dataset. The d_i 's and s_i 's given B are mutually independent, therefore the complete data likelihood is

$$p_c(D, S | B, \{\sigma_{i1}^2, \sigma_{i2}^2; i=1, \dots, N\}) = \prod_{j=1}^N \left[\frac{1}{\sqrt{2\pi\sigma_{j1}^2}} e^{-(d_j - b_j)^2 / 2\sigma_{j1}^2} \cdot \frac{1}{\sqrt{2\pi\sigma_{j2}^2}} e^{-(s_j - (b^{**}p)_j)^2 / 2\sigma_{j2}^2} \right]. \quad (A1)$$

Assuming $\{\sigma_{i1}^2, \sigma_{i2}^2; i=1, \dots, N\}$ are known, we can obtain the complete data log likelihood by taking the logarithm on both sides,

$$L_c(B|D, S) = \sum_{j=1}^N [-(d_j - b_j)^2 / 2\sigma_{j1}^2 - (s_j - (b ** p)_j)^2 / 2\sigma_{j2}^2 - \log \sqrt{2\pi\sigma_{j1}^2} - \log \sqrt{2\pi\sigma_{j2}^2}] \cdot \quad (A2)$$

The EM algorithm is comprised of two steps: one, the E-step, where the expectation of the complete data log likelihood with respect to the present estimate of B is computed, and two, the M-step, where a new estimate of B is obtained which will maximize the computed expectation in the E-step.

First, employ the E-step:

$$Q(B|B^{(n)}) = E[L_c(B|D, S) | Y, B^{(n)}] \quad (A3)$$

$$= \sum_{j=1}^N \{ -(b_j^2 - 2d_j^{(n)}b_j) / 2\sigma_{j1}^2 - [(B ** P)_j]^2 - 2s_j^{(n)}(B ** P)_j / 2\sigma_{j2}^2 \\ + \text{terms} \cdot \text{independent} \cdot \text{of} \cdot B \},$$

where $d_j^{(n)} = E[d_j | Y, B^{(n)}]$ (A4)

$$s_j^{(n)} = E[s_j | Y, B^{(n)}]$$

Second, the M-step to find $B^{(n+1)}$ that will maximize $Q(B|B^{(n)})$:

$$\frac{\partial Q(B|B^{(n)})}{\partial b_k} = 0 = -(2b_k - 2d_k^{(n)}) / 2\sigma_{k1}^2 - \sum_{j=1}^N [2(B ** P)_j p_{jk} - 2s_j^{(n)} p_{jk}] / 2\sigma_{j2}^2 \cdot$$

Solving the above equation for b_k gives

$$b_k^{(n+1)} = d_k^{(n)} - \sigma_{k1}^2 \sum_{j=1}^N p_{jk} \cdot [(B^{(n+1)} ** P)_j - s_j^{(n)}] / \sigma_{j2}^2 \cdot \quad (A5)$$

Using $B^{(n)}$ to approximate $B^{(n+1)}$ in the right-hand side yields

$$b_k^{(n+1)} = d_k^{(n)} - \sigma_{k1}^2 \sum_{j=1}^N p_{jk} \cdot [(B^{(n)} ** P)_j - s_j^{(n)}] / \sigma_{j2}^2 \cdot \quad (A6)$$

As a good estimate of the primary image is formed, $(B^{(n)} ** P)_j - s_j^{(n)} \approx 0$, then,

$$b_k^{(n+1)} \approx d_k^{(n)}. \quad (A7)$$

The same apparent form was obtained for Poisson noise model in Reference 2. But due to the different statistical models, the actual forms of $d_k^{(n)}$ are different and so is the iterative formula for b_k .

Equation (A7) combines with equation (A4) to give the following updated equation:

$$b_k^{(n+1)} = b_k^{(n)} + w_k \cdot [y_k - (b_k^{(n)} + (B^{(n)} ** P)_k)], \quad (A8)$$

where

$$w_k = \sigma_{k1}^2 / (\sigma_{k1}^2 + \sigma_{k2}^2). \quad (\text{A9})$$

REFERENCES

- ¹ R. S. Saunders, Jr. and E. Samei, "A Monte Carlo Investigation on the Impact of Scattered Radiation on Mammographic Resolution and Noise," Proc. SPIE 6142, 3A1-7 (2006).
- ² A. H. Baydush, J. E. Bowsher, J. K. Laading, and C. E. Floyd, Jr., "Improved Bayesian Image Estimation for Digital Chest Radiography," Med. Phys. 24 (4), 539 - 545 (1997).
- ³ B. R. Whiting, "Signal Statistics of X-ray Computed Tomography", Proc. SPIE 4682, 53-60 (2002).
- ⁴ S.Z. Li, "On Discontinuity-Adaptive Smoothness Priors in Computer Vision", *IEEE Transactions on Pattern Analysis and Machine Intelligence*, 17(6), 576-586 (1995).
- ⁵ T. Hebert and R. Leahy, "A Generalized EM Algorithm for 3D Bayesian Reconstruction from Poisson Data Using Gibbs Priors," IEEE Trans. Med. Imag. 8, 194 - 202 (1989).